REVIEW

Composite solid electrolytes: recent advances and design strategies

N. F. Uvarov

Abstract The physical properties of composite solid electrolytes are briefly reviewed. The surface potential formation and the point defects equilibrium at free surfaces and interfaces are considered in frames of the unified Stern model. Special attention is drawn to true size effects due to the change of the bulk characteristics of ionic salts in the nanocomposites. The main thermodynamic reason of the nanocomposite formation relates to the adhesion energy, γ_a. At sufficiently high γ_a values, the ionic salt tends to spread along the oxide surface and to form a nanocomposite if the oxide is nanocrystalline or nanoporous. Analysis of the experimental data shows that non-autonomous interface phases, crystalline or amorphous, exist in some composites. The reason for the stabilization of non-equilibrium states is the complex influence of several factors, including the interfacial interaction between components, particle size effect, and elastic strains in the lattice of the ionic salt. The results of molecular dynamic simulations show that the main origins of the conductivity enhancement are the adsorption of ions to oxide surface with the formation of a space charge layer, the lattice deformation near interface, and an appearance of interdomain boundaries generated by misfit dislocations. The equations proposed earlier for the conductivity description are analyzed. Among them, the general mixing rule has a rather simple analytical form and provides appropriate description of the experimental data on both ordinary insulator–conductor composites and composite solid electrolytes in a broad concentration range. Main approaches for the improvement or creating new composite systems are analyzed.

Keywords Ionic salts · Interface phases · Nanocomposites · Ionic conductivity

N. F. Uvarov (✉)
Institute of Solid State Chemistry and Mechanochemistry,
Siberian Branch of the Russian Academy of Sciences,
Kutateladze 18,
Novosibirsk 630128, Russia
e-mail: uvarov@solid.nsc.ru

Introduction

Composite solid electrolytes of the ionic salt–oxide (MX–A) type can be considered as a new class of ionic conductors with high ionic conductivity which occurs via interfaces. The combination of high conductivity with the enhanced mechanical strength together with the wide prospects for the purposeful modification of the electrolyte properties by varying the type and concentration of the dopant makes these composites promising materials for real electrochemical systems. Since the pioneering paper of Liang published in 1973 [1], a large number of composite ionic conductors were studied in the subsequent years. Actually, heterogeneous doping with dispersed oxides (as heterogeneous dopants) was shown to enhance the conductivity of virtually all composites based on classical (non-superionic) ionic salts, i.e., it is a general effect which requires scientific explanation and theoretical substantiation. There are several reviews devoted to the description and the analysis of the ion transport in polycrystalline and composite solid electrolytes [2–25]. The increase in the ionic conductivity upon heterogeneous doping can be explained within the framework of the space charge model proposed by Wagner and Maier [3, 4, 8–10, 18–19, 22, 26]. This model allows the interpretation of many phenomena observed in composites and is the best suited for the explanation of experimental data for composites containing oxides with relatively coarse grains. However, the space

charge model in its classical version is correct only for ideal crystals in contact with vacuum or a structure-free medium and obviously ignores the real features of the interphase contact, namely, changes in the structures of ionic crystals (e.g., for epitaxial contacts), the effect of elastic strains, the formation of dislocations, etc. Moreover, if the surface concentration of defects is sufficiently high, it is impossible to ignore the interaction between the defects, which results in their ordering and the formation of superstructures and even metastable surface phases. It is known that the conductivity of composites increases as the size of dopant particles decreases. Hence, composites with nanosized grains (about 10 nm) are of particular interest for practice. Obviously, uniform mixing of such an oxide with an ionic component should produce a nanocomposite the properties of which strongly depend on the energy of surface interaction and the peculiarities of the interface between the phases. For composites with coarse-grained additives, the presence of surfaces or interphase contacts has virtually no effect on the bulk properties of the ionic salt; hence, the increase in the conductivity is purely of surface nature. However, in many cases, it still remains unclear whether the enhanced conductivity is primarily caused by the specific interactions at the interface or by the trivial increase in the surface conductivity as such. To answer this question, information on the conductivity of polycrystals is necessary. In nanocomposites, an ionic salt is virtually totally located at the interface. Therefore, its structure and thermodynamic characteristics can substantially change. Particularly, for ionic compounds containing high-temperature disordered phases, the latter may prove to be stable at low temperatures in nanocomposites. Therefore, it is important to understand the thermodynamic reasons for the stabilization of a disordered phase.

In this review, the quasi-chemical mechanisms of the interfacial interaction, problems of thermodynamic stability of nanocomposites, and the genesis of the composite morphology during its sintering are discussed. Properties of ionic salts are analyzed for a wide series of systems with an emphasis on size effects in nanocomposites. Methods for the qualitative estimation of conductivity and other physicochemical characteristics of composites are considered, and approaches for the development of novel composite systems are reviewed and discussed.

Interface interaction and point defect equilibrium

The main reason for the change in the physical properties of ionic salts in composites is the interface interaction between the components of the composite: ionic salt MX and oxide A. In terms of quasi-chemical approach, strong ion–ion interactions may be represented as a process of the chemical adsorption of ions to the oxide surface [4, 8]. From general conditions of mass and charge conservation, it follows that concentrations of ions are interrelated to fractions of corresponding point defects. As the conductivity in ordinary ionic salt MX occurs via migration of point defects, it is convenient to express the parameters of the chemical adsorption of ions in terms of the adsorption isotherms of the corresponding defects (including impurity ions) of i-th type with the adsorption energies of Δg_i. Chemical adsorption of charged species seems to be a general phenomenon typical for any polar media (including ionic crystals) and may take place for both free surfaces of MX, grain boundary MX–MX, and MX–A interfaces. Therefore, the same phenomenological model can be applied to surface or interface-related effects in polycrystalline samples and composites. Such approach is known in electrochemistry as the Stern model [27]. This model may be used for estimation of the surface potential [28, 29], a key factor determining the concentration profile of the defects near the surface.

Defects on free surface of an ionic crystal

In ionic salts, there is the lattice distortion associated with the asymmetric field at the surface. As a result, all characteristics of point defects and impurity ions located on the surface differ from those in the bulk. Their difference is the reason for the specific adsorption of defects at the crystal surface. If the adsorption energies Δg_i of oppositely charged defects are different, then an excess number of defects that have the most negative value of Δg_i appear on the surface. Defects of the opposite charge form a diffuse layer, or space charge layer (SCL), under the surface. According to the Stern model, the surface charge Q_S is determined by the sum of contributions made by all defects adsorbed on the surface. In the simplest case of the Langmuir adsorption isotherm, the surface charge is given by an expression [27]:

$$Q_S = \sum_i q_i N_{S,i} \times \left[1 + \frac{N_i}{n_{\infty,i}} \times \exp\left(\frac{\Delta g_i + q_i \varphi_S}{kT} \right) \right]^{-1},$$
(1)

where $N_{S,i}$ is the concentration of available surface sites (adsorption centers); q_i is the effective charge of the defect, $n_{\infty,i}$ is the concentration of the defects in the bulk of the crystal; and N_i is the concentration of the i-th type regular sites of the crystal lattice; the summation is done over all possible charged defects of i-th type. As follows from Eq. 1, the surface charge is determined by both the bulk properties $(n_{\infty,i})$ and surface-related parameters: the adsorption energies Δg_i and the surface potential φ_S which is approximately equivalent to the potential at inner Helmholtz layer in

electrochemistry. The surface charge is balanced by the charge of the SCL, Q_d, formed under the crystal surface. If the probability of finding an ion at a particular point depends on the local potential through a Boltzmann distribution, $n_i(x) = n_{i,\infty} \cdot \exp(-q\varphi(x)/kT)$, then the charge density distribution and the potential gradient must satisfy the Poisson–Boltzman equation. The solution of this equation is the Gouy–Chapman formula for the charge of SCL:

$$Q_d = A \times \left\{ \sum_i n_{\infty,i} \times \left[\exp\left(-\frac{q_i \times \varphi_{s-1}}{kT} \right) - 1 \right] \right\}^{1/2}, \quad (2)$$

where $A = (2\varepsilon\varepsilon_0 kT)^{1/2}$; φ_{S-1} is the potential of the outer Helmholtz layer. Assuming that in first approximation $\varphi_S = \varphi_{S-1}$, one may determine its value from the overall electroneutrality condition $Q_S + Q_d = 0$ and Eqs. 1 and 2. From these equations, it is seen that the absolute value of the surface potential in pure MX crystal depends on four independent parameters: two values of Δg_i, total concentration of point defects in the bulk $n_{\infty,i}$ (defined only by the defect formation energy g_0), and the concentration of available surface sites N_S (assumed that $N_{S,i}$ values for both types of defects are equal to N_S). Calculated values of the surface potential for a model crystal of NaCl-type with Schottky defects and superionic oxides $M^{IV}_{1-c}Me^{III}_cO_{2-c/2}$ have been reported elsewhere [28]. Figure 1 shows typical temperature dependences of the surface potential for a crystal of the NaCl-type with the Schottky defects doped with the impurities of
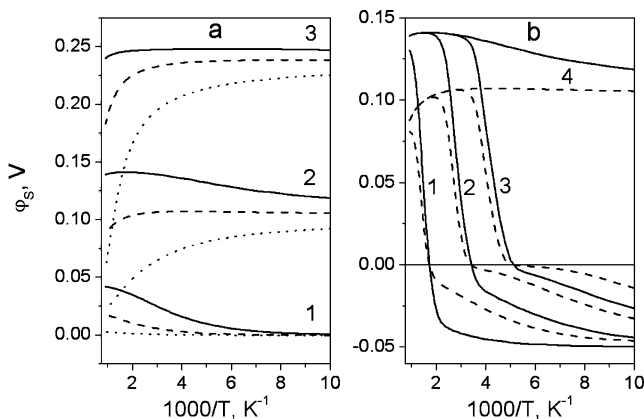

Fig. 1 Dependences of the surface potential on the reciprocal temperature for the crystal of the NaCl-type with Schottky defects. a For pure crystal at $\Delta g^+ = -0.1$ eV and $\Delta g^- = -0.2$, -0.4, and -0.6 eV, curves 1, 2, and 3, respectively; solid, dashed, and dotted lines correspond to the concentration of the surface adsorption sites of 10^{15}, 10^{14}, and 10^{13} cm^{-2}, respectively. b For crystal doped with the impurities of bivalent metals at $\Delta g^+ = -0.1$ eV, $\Delta g^- = -0.4$ and zero segregation energy, the molar fraction of the dopant is 10^{-3}, 10^{-6}, and 10^{-9} for curves 1, 2, and 3, respectively; curve 4 corresponds to the ideally pure crystal; solid and dashed lines correspond to the concentration of the surface sites of 10^{15} and 10^{14} cm^{-2}, respectively; defect association effects in the bulk of the crystal are neglected. The defect formation energy, g_0, is equal to 1 eV; all energies, g_0, Δg^+, and Δg^-, are taken to be independent of temperature

bivalent metals. Recently, the surface potential in superionic oxides was estimated using different equations for different charge distribution in SCL (Gouy–Chapman or Mott–Schottky) [29]. The temperature dependences $\varphi_S(T)$ for these systems are presented in Fig. 2. The obtained results may be summarized as follows:

– the surface potential is non-zero only if at least one of $\Delta g_i < 0$ and is determined by the difference in the defect adsorption energies Δg^- and Δg^+ of positively and negatively charged dominant defects. If $\Delta g^- = \Delta g^+$ then $\varphi_S = 0$;

– the surface potential monotonically increases with N_S value;

– in pure ionic crystal, the temperature behavior of φ_S depends on the value of Δg^α, (where Δg^α energy is the most negative of Δg^+ and Δg^- ones) and differs for two cases: (a) $|\Delta g^\alpha| < g_0/4$; the surface potential is small, φ_S monotonically increases with the temperature and rises as a function of the defect concentration in the bulk and N_S; (b) $|\Delta g^\alpha| > g_0/4$; the case of high surface potentials. The values of φ_S may increase or decrease with temperature as a function of N_S values. At sufficiently high values of the adsorption energy $|\Delta g^\alpha|$ and N_S, the surface potential decreases with temperature and does not depend on the defect concentration;

– at high N_S and $|\Delta g^\alpha|$, the surface potential tends to the value of $\varphi_S \approx (\Delta g^- - \Delta g^+)/2e$, which can be regarded as the upper limit. It is to be noted that this expression is formally similar to the equation $\varphi_S \approx -(g^- - g^+)/2e$ obtained in frames of the Frenkel–Kliever approach [30–34] where g^- and g^+ are the defect formation energies in the bulk of the crystal.

– in MX crystal doped with MeX$_2$, a situation is more complicated: φ_S values depend on the type, concentration of the impurity ions [given by the energy of dissociation of complexes (impurity ion–cation vacancy)] and their adsorption energy (or segregation energy) Δg^+_{Me}. At $|\Delta g^+| > |\Delta g^-| > |\Delta g^+_{Me}|$ or $|\Delta g^+_{Me}| > |\Delta g^+| > |\Delta g^-|$ (Δg^+, Δg^-, $\Delta g_{Me} < 0$) an isoelectric point (i.e., temperature where φ_S change sign) exists on the $\varphi_S(T)$ dependence;

– in superionic oxides, $M^{IV}_{1-c}Me^{III}_cO_{2-c/2}$ values of φ_S are generally bounded by limiting parameters given by Δg^+ and Δg^-_{Me} (the adsorption energy of oxygen vacancies and the segregation energy of Me cations, respectively). The values of φ_S obtained using Gouy–Chapman and Mott–Schottky models of SCL strongly differ in the low temperature limit and are very close at high temperatures. Therefore, at high temperatures, the surface potential is practically independent of the particular form of the $\varphi(x)$ function in SCL and is
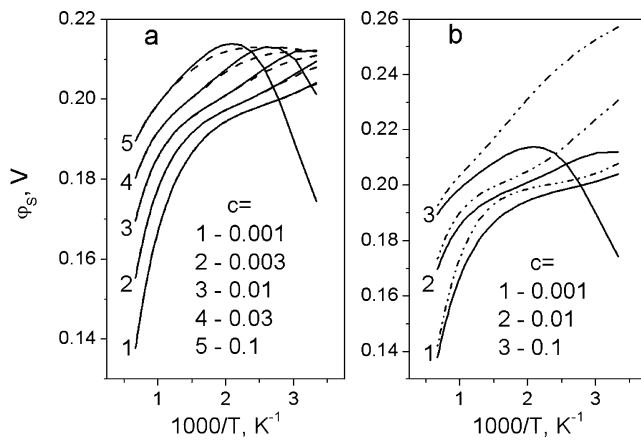
Fig. 2 Dependences of the surface potential on the reciprocal temperature for the superionic oxide $Zr_{1-c}Me_cO_{2-c/2}$ calculated using the Stern model with Gouy–Chapman and Mott–Schottky potential distribution in the space charge at $\Delta g^- = 0$; $\Delta g^+ = -0.6$ eV and zero segregation energy. **a** Curves calculated with Gouy–Chapman model at different concentration of the dopant, c; *solid lines* correspond to the case of non-associated defects, whereas *dashed lines* are calculated assuming that uncharged complexes $[2Me–V_O]^x$ form with the association energy of 0.4 eV. **b** The curves obtained using Gouy–Chapman and Mott–Schottky models (*solid and dash-dotted lines*, respectively) at different dopant concentrations

energy necessary for generation of a single defect. This value is constant only within certain temperature ranges corresponding to intrinsic or extrinsic conductivity regions. Table 1 lists $g_i^\pm$ values in the bulk of the crystal of MX doped with MeX_2 impurity in three temperature regions. Using these data, one can plot energy diagrams (Fig. 3) illustrating the difference between the defect energies in the bulk of the crystal and at the surface for MeX_2-doped MX crystal in different temperature ranges. This diagram differs from the diagrams reported earlier [13, 19, 34], as in the bulk of the crystal in the intrinsic region, the defect formation energies for both the defects are taken to be equal to $g_0/2$. As seen from the diagram, at negative values of adsorption energies, the surface is enriched in defects even in the case of zero surface charge (it is possible at $\Delta g^+ = \Delta g^-$). In general, the surface can be considered as an independent subsystem characterized by intrinsic surface disordering with an effective defect formation energy equal to $g_s = g_0 + (\Delta g^+ + \Delta g^-)/2$. The surface is more or less disordered than the bulk (i.e., enriched or depleted in defects on average) depending on the sign of the second term of this equation.

Defects on the interface

First, let us consider the interface between ionic salt MX and A. In this case, the concentration of defects inside the bulk of oxide is negligible and only first oxide layer takes part in the interface interaction which includes pair interactions between ions of MX and A. This results in changing the defect adsorption energies, the surface potential and, consequently, the concentration of point defects in the diffuse layer, leading to the enhancement of the conductivity of composites. Such mechanism has been proposed by Maier and was discussed in detail in several papers [4, 8, 9]. It has been suggested that the interface interaction consists in a selective chemical adsorption of M^+ cations, i.e., their shift from the MX bulk to the MX–A interface. Physically, it is equivalent to the change in the adsorption energy of positively charged defects (anionic vacancies $V_x^\cdot$ or interstitial cations $M_i^\cdot$) and formation of high positive charge at the interface. As a result, a diffuse layer enriched in cationic vacancies forms near the interface. The energy diagram for MX–A interface is

determined mainly by the adsorption energies of the defects;

– according to the literature data [35–37], in oxides of the $M^{IV}_{1-c}Me^{III}_cO_{2-c/2}$ type, the surface potential is positive; therefore, $\Delta g^+ < 0 (\Delta g^+ > |\Delta g_{Me}^-|)$ and the surface should be enriched in anionic vacancies and depleted in cations. Within the Stern model, the adsorption of oxygen vacancies and the segregation of extrinsic cations are interrelated, and even at $\Delta g_{Me}^- = 0$, a strong segregation of cations on the surface takes place. Nevertheless, the surface as a whole remains positively charged and the diffusion layer is depleted of anionic vacancies.

Representing the chemical potential of i-th defects, μ_i, in the standard form, $\mu_i = g_i^\pm + kT \cdot \ln []_i$ (here $[]_i$ is the fraction of the defects; superscript corresponds to the sign of the defect), and taking into account the electrical neutrality condition, one can obtain values of $g_i^\pm$ for all the defects. Physically, each $g_i^\pm$ value corresponds to the

Table 1 The standard values of chemical potential $g_i^\pm$ for cation vacancy, g^-, anion vacancy, g^+, and impurity cations, g_{Me}^+ at different temperature regions for MX crystal with Schottky defects

Defect	Notation	Extrinsic region, low temperatures	Extrinsic region, high temperatures	Intrinsic region
Cation vacancy, V_M'	G^-	$g_d/2 + 1/2 \times kT \times \ln c$	$-kT \times \ln c$	$g_0/2$
Anion vacancy, $V_X^\cdot$	g^+	$g_0 - g_d/2 - 1/2 \times kT \times \ln c$	$g_0 - kT \times \ln c$	$g_0/2$
Impurity cations, $Me_M^\cdot$	g_{Me}^+	$g_d/2 + 1/2 \times kT \times \ln c$	$-kT \times \ln c$	$-kT \times \ln c$

g_0 Schottky defect formation energy, g_d energy of dissociation of complexes $[V_M' - Me_M^\cdot]^x$, c concentration of impurity MeX_2

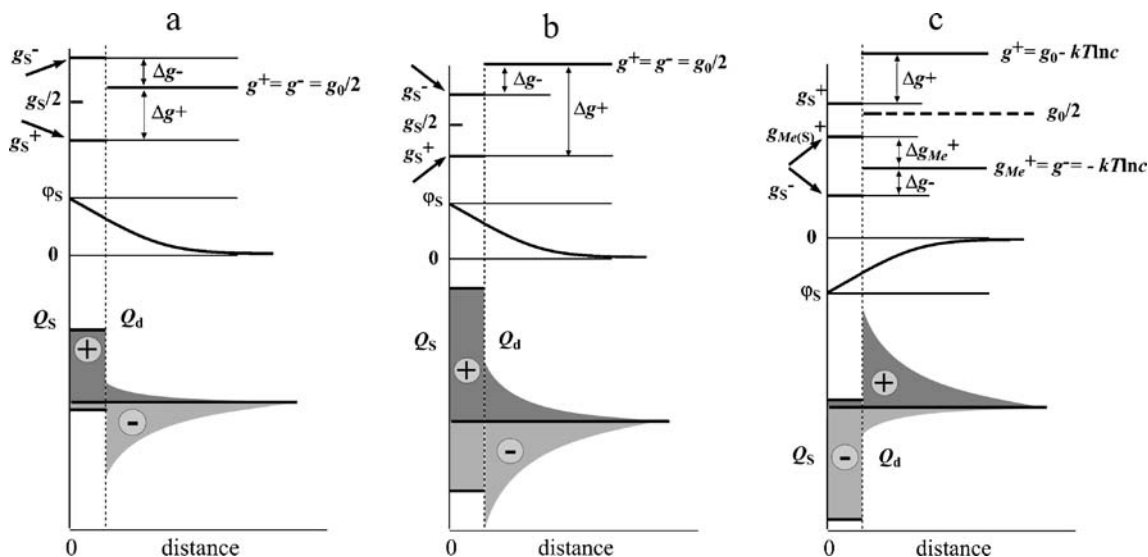**Fig. 3** Energetic diagrams of surface and bulk defects, the potential profiles, and the charge distribution near the surface of the pure (**a**, **b**) and doped (**c**) ionic crystal MX with Schottky defects. The diagrams obtained in terms of the Stern model. Cases **a** and **b** correspond to the pure crystal with different Δg^+ and Δg^- values. Cases **b** and **c** relate to the MX crystal doped with bivalent impurity MeX_2 (the dopant concentration is equal to c) in intrinsic (**b**) and extrinsic (**c**) conductivity regions. Energies which determine the surface potential are indicated by bold arrows

presented in Fig. 4a. Selective adsorption of cations can be regarded as interaction a Lewis acidic of M^+ cations with the basic O^{2-} or OH^- centers on the oxide surface. Therefore, the adsorption energy should depend on the type of cation (acidity of the cation increases with the decrease in the ionic radius) as well as on the presence and strength of basic groups on the oxide surface. The concentration of charge carriers on the surface or interface region of MX can be varied due to the modification of the surface by electronic donor molecules [38, 39].

Recently, we have carried out a comparative study of electrical properties and ^7Li NMR data of the composites $LiClO_4–A$ (A = α-Al_2O_3, γ-Al_2O_3, α-$LiAlO_2$, γ-$LiAlO_2$) [40, 41]. It was shown that the conductivity depends not only on the specific surface but also on the chemical nature and the structure of the additive: At the same value of the specific surface area, composites with γ-Al_2O_3 and γ-$LiAlO_2$ have lower activation energy of conductivity than the composites containing α-Al_2O_3 and α-$LiAlO_2$ additives. Possible mechanism of such behavior may originate
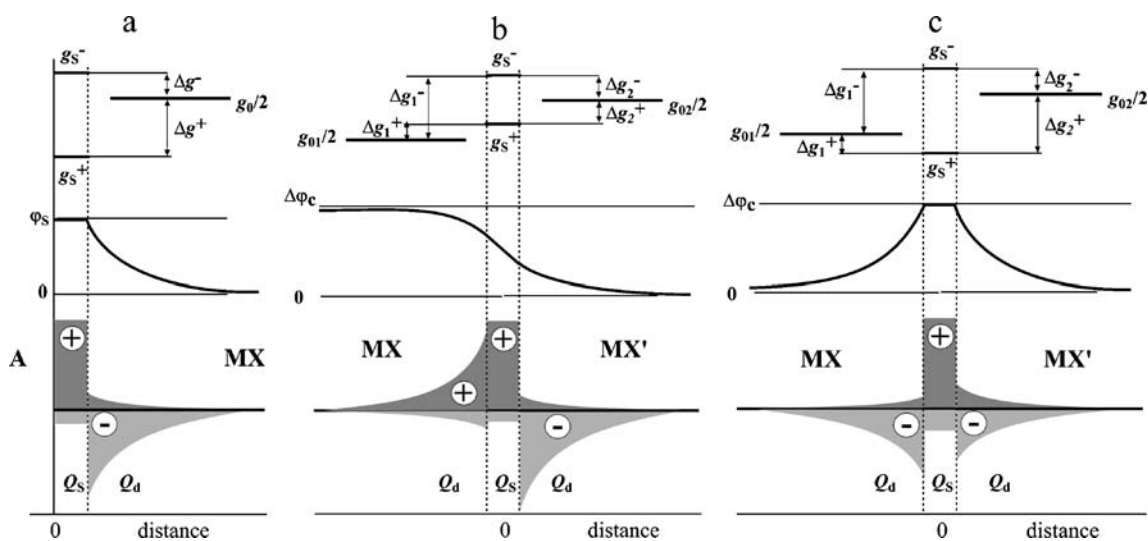

Fig. 4 Energetic diagrams of surface and bulk defects, the potential profiles, and the charge distribution near the MX–A (**a**) and MX–MX' (**b**, **c**) interfaces. The diagrams obtained in terms of the Stern model. Cases **b** and **c** differ by the values of Δg^+ and Δg^-

from the difference in the crystalline structure of oxides that influences the structure and transport properties of the LiClO$_4$–A interface. The presence of large number of mobile lithium ions in the composites was confirmed by ^{7}Li NMR.

In heterogeneous systems consisting of two ionic salts (of the MX–M′X type), there are diffuse layers in both phases. Therefore, for the calculation of the surface potential using the Stern model, one has to take into account the adsorption of defects in each phase to their common interface. Such a situation is demonstrated in the energy diagram depicted in Fig. 4b,c for the contact of two intrinsic conductors MX and MX′ with Schottky defects. In this case, the surface potential is determined by six independent parameters: (1) the defect formation energies in the bulk of the phases MX and MX′, g_{01} and g_{02}, respectively; (2) the energies Δg_1^+ and Δg_1^- of the defect adsorption for one of the phases (the corresponding adsorption energies for another phase are given by relations $\Delta g_2^+ = (g_{01} + g_{02})/2 - \Delta g_1^+$ and $\Delta g_2^- = (g_{01} + g_{02})/2 - \Delta g_1^-$); (3) the number of active surface sites, N_S; and (4) the potential difference between MX and MX′, or Galvani potential, $\Delta\varphi_c$, which cannot be measured directly. The work is in the progress for analysis the Stern equation for this case. Preliminary estimations show that the following qualitatively different situations, demonstrated in Fig. 4b,c may be realized:

- if $\Delta g_i^{\pm} > 0$, then the interface charge is close to 0, two oppositely charged diffuse layers may be formed due to the existence of the potential drop between the phases. Such potential profile (Fig. 4b) is typical for a classical semiconductor–liquid electrolyte boundary [42, 43] and has been applied to the explanation of interface-related properties of MX–MX′ systems by Maier [13, 44];
- if $\Delta g_i^{\pm} < 0$, the surface potential and the interface charge are high; the potential has an extremum at the interface; two double layers form near the interface in both the phases with the space charge opposite in sign to the interface charge. Such profile is presented in Fig. 4c; it is qualitatively similar to one at intergrain boundaries of ionic crystals, but the charge distribution is not symmetrical: Higher space charge is accumulated in the phase with lower value of the defect formation energy.

These variants correspond to some limiting cases. The real situation is intermediate and the interface potential is defined by all independent parameters mentioned above. In the case of the doped ionic crystals, one can also take into account the concentration of dopants in the contacting phases and the segregation energy of dopants to the interface. As no data on the interface potential the MX–MX′ systems are available in the literature, it is difficult to verify the model.

Thermodynamic description and stability criteria

The interface interaction includes two principal terms: contribution of inter-atomic interactions between ions or atoms of adjacent phases MX and A and the contribution of the elastic energy of mechanical strains emerging inside the crystal lattice of the ionic salt near the interface due to the misfit in lattice parameters of the contacting phases. The interface interaction is characterized by the interface energy γ_{MX-A} which is usually expressed as [45]:

$$\gamma_{MX-A} = \gamma_{MX} + \gamma_A - \gamma_a, \tag{3}$$

where γ_{MX} and γ_A are standard surface energies of MX and A, respectively, and γ_a is the adhesion energy. Free Gibbs energy of the mixture of the ionic salt MX and dispersoid A is given by a sum:

$$G = \left(G_{MX}^0 + \gamma_{MX}S_{MX} + G_{MX}^{str}\right)$$
$$+ \left(G_A^0 + \gamma_A S_A + G_A^{str}\right) + \gamma_{MX-A}S_{MX-A}, \tag{4}$$

which includes standard values of the Gibbs energy of i-th component G_i^0; the surface contribution $\gamma_i S_i$ (γ_i is the average value of specific surface energy; S_i is the total area of free surface of i-th component); excess elastic energy due to lattice strains G_i^{str}; and the contribution of the interface energy, $\gamma_{MX-A}S_{MX-A}$, where S_{MX-A} is the interface area.

There are two variants of the changes in MX morphology on sintering [25, 46, 47]:

- If $dG/dS_{MX-A} > 0$, then the decrease in the MX–A interface area is favorable and trivial processes of MX recrystallization and grains coarsening take place by the Oswald "ripening" mechanism;
- In the alternative case $dG/dS_{MX-A} < 0$, it is energetically favorable for system to expand the interface area by spreading of MX along free A surfaces. With Eqs. 3 and 4, neglecting the lattice strain energies G_i^{str}, the condition $dG/dS_{MX-A} < 0$ may be represented as:

$$dG/dS_{MX-A} = \gamma_{MX} \times (dS_{MX}/dS_{MX-A}) + \gamma_A$$
$$\times (dS_A/dS_{MX-A}) + \gamma_{MX} + \gamma_A$$
$$- \gamma_a < 0. \tag{5}$$

For ordinary wetting process, when liquid spreads along the plane surface with formation of a film, $dS_{MX}/dS_{MX-A} \approx 1$; $dS_A/dS_{MX-A} \approx -1$ and Eq. 3 reduces to well-known Gibbs–Smith wetting criterion:

$$\gamma_a > 2\gamma_{MX} \tag{6a}$$

which holds for epitaxial growth of thin films on substrates. However, the surface in real composite materials has more

complicated geometry. If highly dispersed oxide is taken as a heterogeneous dopant, it acts like a porous matrix easily impregnated with the ionic salt. In this case, formation of new MX–A interfaces does not lead to generation of new free MX surfaces, so that $dS_{MX}/dS_{MX-A} \approx 0$; $dS_A/dS_{MX-A} \approx -1$ and the wetting may proceed at:

$$\gamma_a > \gamma_{MX}, \tag{6b}$$

i.e., much easier than in two-layer systems. In any case, from Eqs. 6a and 6b, it follows that increase in the adhesion energy as well as the decrease in the MX surface energy favors the wetting effect. The change in morphology of the heterogeneous system as a result of sintering for both $\gamma_a > 2\gamma_{MX}$ and $\gamma_a > \gamma_{MX}$ is schematically shown in Fig. 5. For real systems with undefined morphology, when the spreading is accompanied by generation of strong strains, the conditions 6a and 6b may be represented in a general form:

$$\gamma_a > (2 - \theta) \times \gamma_{MX} + \beta_{MX} + \beta_A \tag{7}$$

where θ is the roughness factor ($0 \leq \theta \leq 1$); $\beta_{MX} = dG_{MX}^{str}/dS_{MX-A}$; $\beta_A = dG_A^{str}/dS_{MX-A}$; β_{MX}, $\beta_A > 0$ due to a misfit between lattice parameters of MX and A; hence, strains hinder the spreading of MX on the surfaces of A. The last two terms seem to increase with the decrease in the grains size of oxide; in particular, this follows from the analysis of X-ray diffraction (XRD) peak broadening which allows estimating both the average crystallite size and lattice deformation. Physically, such situation may be explained by a strong curvature of the oxide surface when its radius becomes comparable with the molecular size or lattice parameter of MX. In this case, the term β_{MX} becomes too large, the condition 7 is not satisfied anymore and spontaneous

spreading does not occur. This effect indeed was observed by Ponomareva et. al. [48, 49] in a series of composites $MHSO_4–SiO_2$ (M = Rb, Cs) where silica had different pore structure. In these samples, the pore size of silica was varied in a wide range of 1.4–300 nm. Note that the conductivity had a maximum as a function of the pore size; the ionic salt easily spread onto large pores and did not penetrate the pores smaller than ~3.5 nm.

After the salt covers all free surfaces of highly dispersed oxide ($S_{MX} \ll S_{MX-A}$), the Gibbs energy of MX changes to the value of:

$$G_{MX}' \approx G_{MX}^0 + \gamma_{MX-A} \times S_A/2 + G_{MX}^{str}$$
$$= G_{MX}^0 + (\gamma_{MX-A} + 2\beta_{MX}) \times S_A/2. \tag{8}$$

For physically reasonable values $\gamma_A > \gamma_a$; $\beta_{MX} > 0$, the interface energy γ_{MX-A} is positive and G_{MX} will increase. The wetting effect should proceed until all free surface of A is covered by the more mobile ionic component MX. If the A particle size is sufficiently small, $L_A \sim 10$ nm, then after prolonged sintering, one can obtain the MX–A nanocomposite where the effective MX grain size of MX (L_{MX}) is close to L_A. Thus, the main reason for such spontaneous self-dispersion and changing physical properties of the ionic salts in nanocomposites MX–A is the interfacial interaction between the phases. It should be emphasized that in contrast to many nanosystems, the nanocomposite formed on the interfacial spreading is thermodynamically stable, i.e., it exists in a local thermodynamically equilibrium state given by the value of the specific surface area (or grain size) of the oxide.
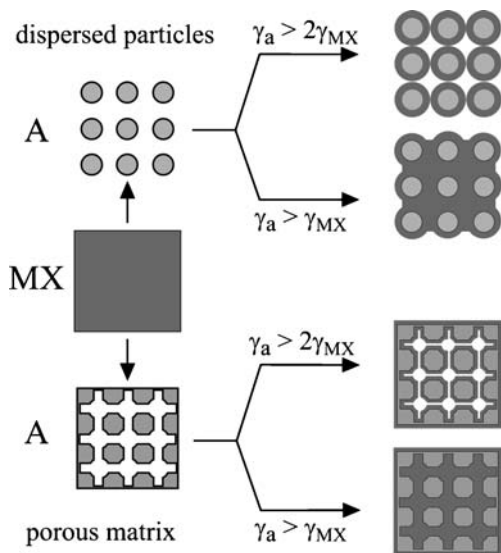
True size effects in nanocomposite solid electrolytes

When the particle size becomes smaller than 10–100 nm, physical properties of solids substantially change. During the last two decades, a significant progress was achieved in the research of various nanosystems such as nanostructured pure and composite materials, metal nanoparticles, carbon nanotubes, mesoporous systems, etc. There are size effects of two types in the heterogeneous systems: trivial one (due to the decrease in the grain size without strong impact of the interface interaction) and true size effect when the interfaces play a crucial role [12, 19, 50]. In this section, the true size effects in nanocomposite electrolytes are only considered.

As follows from Eq. 8, in a composite, the ionic salt has an excess Gibbs energy caused by the influence of MX–A interfaces. The temperature dependencies of Gibbs free energies G_{MX}^0 and G_{MX}' are schematically presented in Fig. 6. One can see that the melting temperature of MX in the composites should be lower than that in pure MX salt. The characteristic grain size, when noticeable deviations in

Fig. 5 The change in morphology on sintering of the mixture of MX with A in the cases of $\gamma_a > 2\gamma_{MX}$ and $\gamma_a > \gamma_{MX}$. The oxide component A is taken in the form of dispersed particles (*upper row*) or porous matrix (*bottom row*)

the thermodynamic properties are observed, is ~10 nm [14, 24, 47, 51–66]. The following approximate relationship for the temperature of a phase transition between high- and

low-temperature MX phases, α and β, can be obtained [24, 101, 116] by equating the values of Gibbs energies:

$$\frac{T_t}{T_t^0} = 1 - \left[\left(\gamma_{MX}^\beta S_{MX}^\beta - \gamma_{MX}^\alpha S_{MX}^\alpha \right) + \frac{1}{2} \left(\gamma_{MX-A}^\beta S_{MX-A}^\beta - \gamma_{MX-A}^\alpha S_{MX-A}^\alpha \right) + \Delta G^{str} \right] \times \frac{1}{H_t} \tag{9}$$

where T_t is the standard temperature of the transition, superscripts α and β correspond to high-temperature and low-temperature phases, respectively, ΔG^{str} is the difference in the strains energies of phases α and β; and H_t is the enthalpy of the phase transition. For pure MX, $S_{MX-A}=0$, whereas for composites with highly dispersed oxides, $S_{MX-A} \gg S_{MX}$ and the second and third terms in brackets prevail. The interface energies γ_{MX} and γ_{MX-A} decrease with temperature; this explains why the transformation temperature should decrease if the phase transition is only accompanied by small changes in volume and ΔG^{str} $\left(S_{MX-A}^\alpha \approx S_{MX-A}^\beta \sim L_A^{-1}; \Delta G^{str} \approx 0 \right)$. The latter situation is indeed usually observed for thin films where the layer thickness plays the role of particle size. According to many experimental observations, the phase transition temperatures in films can decrease by hundreds of degrees as L decreases to 10 nm [51, 52, 61, 65, 66]. Qualitatively similar effects have been observed in nanocomposites CsCl–Al$_2$O$_3$ [67] and CsHSO$_4$–SiO$_2$ [68]: Temperatures of phase transitions (melting or solid state transformation) decrease with the concentration of oxide additive. The temperature of α–β transition in Li$_2$SO$_4$ decreases in Li$_2$SO$_4$–Al$_2$O$_3$ and the transition becomes diffuse [46]. Careful calorimetric studies of $(1-x)$AgI–xAl$_2$O$_3$ [69] nanocomposites show that as x increases, two phase transitions proceed; one occurs at the temperature characteristic of the bulk state, whereas another is observed at a different temperature and is characterized by a strong

hysteresis. The smooth character of the phase transitions and strong hysteresis seem to be a general phenomenon in the nanocomposite systems.

Generally, the phase transition temperatures in a composite can either decrease or increase depending on the particular form of the thermodynamic functions $G_{MX}=f(T)$ and $\Delta G^{str}=f(T)$ in different phases [53, 61, 62]. The literature offers several types of the phase diagrams (Fig. 7a–c) presented as $T_t(L^{-1})$ for different metal films [51, 54, 65, 66]. The cases (c, d) are of special interest as the examples of a strong size effect when new phases unusual for the pure component are stabilized in thin films. Such effects are observed in Al$_2$O$_3$ [70], ZrO$_2$ [71, 72], and TiO$_2$ [73]: Crystals of these oxides smaller than 10–20 nm form metastable (γ-, δ-, θ-Al$_2$O$_3$) anatase TiO$_2$ or high-temperature (t-, c-ZrO$_2$) polymorphs. Most experimental observations in the heterogeneous systems like AgI–Al$_2$O$_3$ [69, 74], MNO$_3$–Al$_2$O$_3$ (M = Li, Na, K) [75], MNO$_3$–Al$_2$O$_3$ (M = Rb, Cs) [76, 77], RbNO$_3$–SiO$_2$ [78], CsHSO$_4$–SiO$_2$ [48, 49, 79], LiClO$_4$–A (A = Al$_2$O$_3$, LiAlO$_2$, SiO$_2$) [40, 41, 80] may be explained by the appearance of amorphous phases of the ionic salt in the composites. This is evidenced by the following effects:

(a) strong decrease in the integral intensity of XRD peaks of all crystalline phases and appearance of a wide halo on the electron diffraction patterns;

(b) decrease of molar enthalpies of all phase transitions in MX, including the melting enthalpy. Instead, a diffuse

Fig. 6 Temperature dependencies of Gibbs free energies of ionic salt in standard conditions (*solid lines*) and in nanoparticles (*dashed lines*). Solid phases and melt are denoted by symbols α, β, and m, respectively. In the cases **b** and **c**, phase β does not exist in normal conditions but appears in the nanosized particles
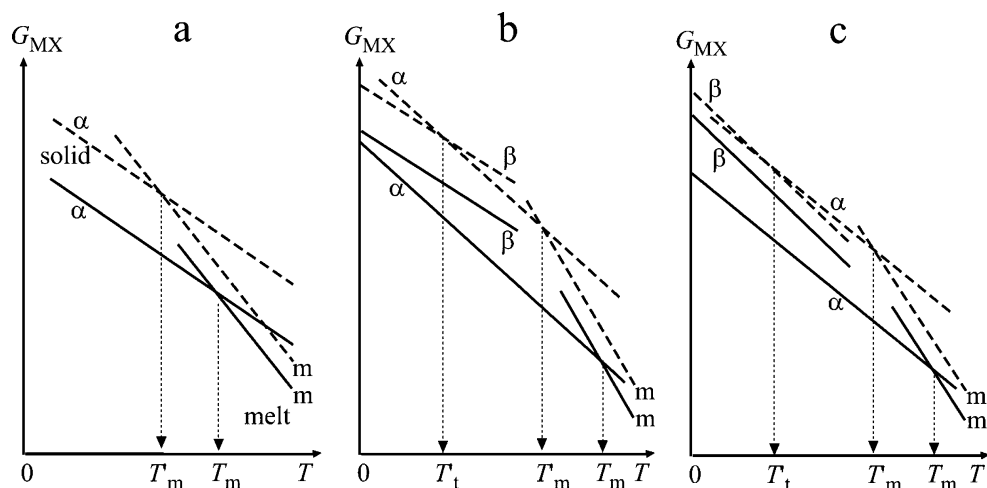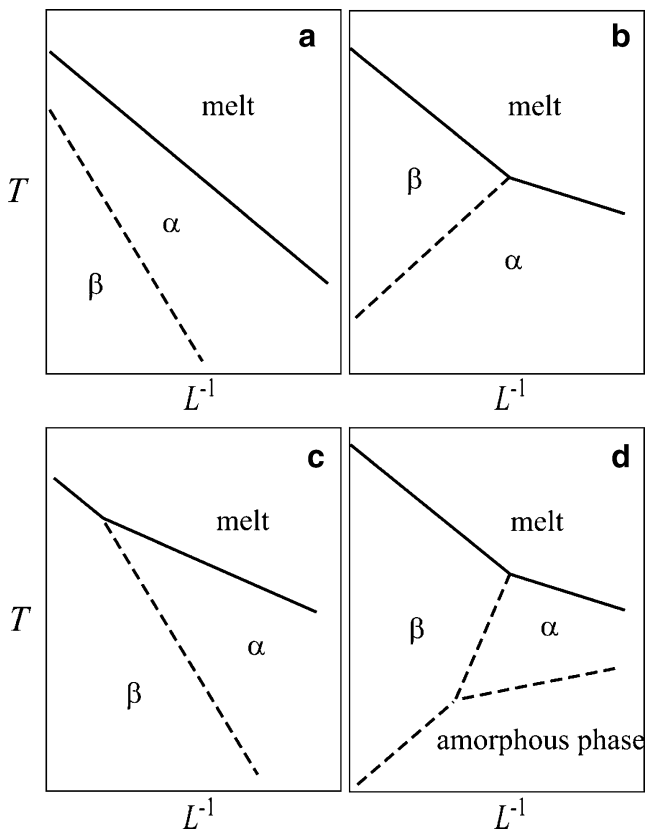
Fig. 7 Phase diagrams represented in coordinates $T_t(L^{-1})$ for films of different metals deposited on supports [51, 54, 65, 66]

peak appears on differential scanning calorimetry (DSC) curves at temperatures much lower than the melting point;

(c) a disappearance of abrupt conductivity changes due to MX phase transitions in the MX–A composites. The Arrhenius conductivity plots are nonlinear for some nanocomposites where the estimated charge-carrier concentration is comparable to the overall number of cations [12], as typical for the superionic conductors or ion-conducting glasses. This is also confirmed by an absence of the conductivity changes on melting; and

(d) effects (a), (b), and (c) systematically become more pronounced when the total number of MX–A interfaces increases. This suggests that the amorphous phase is interface-induced (non-autonomous) and is only located at the MX–A interfaces.

The volume and molar fractions of the interfacial phase (including amorphous one), f_S and x_S, respectively, its thickness (λ), and the fraction of residual bulk phase of MX, f_{bulk} (or x_{bulk}) may be estimated using the brick wall model [12, 17, 25, 69, 77]:

$$f_S = 2\beta\left(\frac{\lambda}{L_A}\right)f(1-f); \qquad f_{bulk} = 1 - f - f_S; \;(f_{bulk} \geq 0) \tag{10}$$

$$x_S = 2\beta\left(\frac{\lambda}{L_A}\right)\frac{\delta x(1-x)}{[1 + x(\delta - 1)]}; \qquad x_{bulk} = 1 - x - x_S; \;(x_{bulk} \geq 0) \tag{11}$$

where the parameter β depends on the morphology of the composite (for cubic blocks $\beta \approx 3$); f (or x) is the total volume (or molar) fraction of oxide; $\delta = \mu_A\rho_{MX}/\mu_{MX}\rho_A$, where μ_i and ρ_i are molecular weights and densities of the components, respectively. The values of x_{bulk} may be determined from the integral intensities of DSC peaks corresponding to phase transitions (including melting). Figure 8 compares the relative molar fractions of ionic salt not transformed into the amorphous state, $x_{bulk}/(1-x)$ in the composites RbNO$_3$–Al$_2$O$_3$ [77], AgI–Al$_2$O$_3$ [69] with a highly dispersed alumina having the specific surface area of 200–270 m^2/g and the data on AgI–Al$_2$O$_3$ prepared with γ-alumina (grain size of 0.06 μm) [81]. The theoretical dependences obtained from Eq. 11 provide good fit to the data. The values of λ obtained by fitting are 3 and 4 nm for AgI–Al$_2$O$_3$ [69] and RbNO$_3$–Al$_2$O$_3$ [77], respectively, and 7 nm for AgI–Al$_2$O$_3$ [81] composites obtained with another alumina modification. At sufficiently high concentrations of the highly dispersed alumina ($x > 0.6$–0.7, or $f > 0.5$–0.6), the effective size of MX particles is comparable with λ, and virtually the whole volume of the ionic salt is in the amorphous state.

The self-dispersion proceeds at significant rates even at temperatures substantially below the MX melting point, i.e., when the ionic salt is in the crystalline state. Due to the solid-phase spreading, the crystalline phase spontaneously
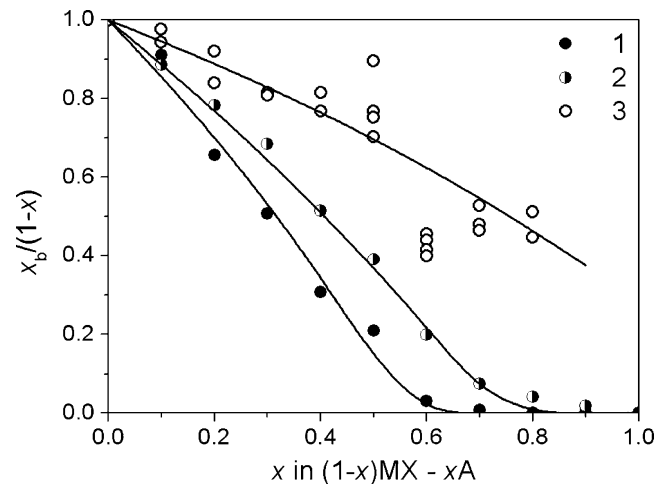

Fig. 8 The relative molar fraction of ionic salt not transformed into the amorphous state, $x_{bulk}/(1-x)$ in composites RbNO$_3$–Al$_2$O$_3$ [77] and AgI–Al$_2$O$_3$ [69] with highly dispersed alumina (the specific surface area of 200–270 m^2/g) (points *1* and *2*, respectively) and the data reported in the literature [81] for AgI–Al$_2$O$_3$ composites prepared with the γ-alumina (the grain size of 0.06 μm). Lines are obtained using Eq. 11 at λ=4, 3, and 7.2 nm for curves *1*, *2*, and *3*, respectively

transforms into the amorphous state. One possible reason for the spontaneous amorphization due to liquid phase or solid phase spreading could be the relaxation of elastic strains that arise in the MX bulk because of the salt spreading over the surface and in the pores of oxide matrix. If the lattices of the contacting phases do not match one another, the contribution of the elastic energy becomes substantial. Moreover, in contrast to thin films, the MX particles in nanopores are adhesively bound with the randomly oriented oxide surfaces surrounding a pore, which should lead to the rather active formation of microdomains and provide the excess surface energy. Apparently, the structural relaxation can occur by spontaneous amorphization of an ionic salt. Crystal phase may relax into more stable amorphous state with larger particles; the increase in the effective particle size from L'' to L' may be due to the change in the particles shape from polyhedral to smooth one. This process may be illustrated by a phase diagram shown in Fig. 9 [25, 82, 83]. A concept of the spontaneous transition from the crystalline to amorphous state was discussed earlier in the context of reasons responsible for mechanical alloying [84–89]. The data on amorphization of alkali metal halides [90, 91] and other inorganic crystalline hydrates [92–94] in nanopores are available. The amorphous hydrates incorporated into nanoporous matrices exhibit unusual thermodynamic properties relevant for the changes in hydration and dehydration [92–94].

The composites MX–A exhibit an enhanced conductivity at temperatures below melting point or superionic phase transition in MX [2–25]. The conductivity goes through a maximum at 20–50 vol.% of the oxide and is qualitatively
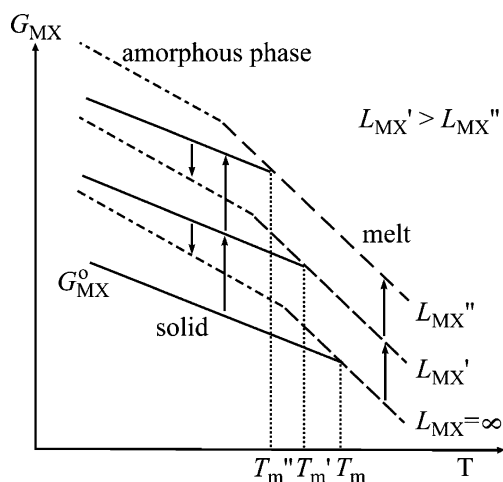

Fig. 10 Dependences of conductivity of nanocomposites $(1-x)$AgI–xAl$_2$O$_3$ [74, 100] (**a**, **b**) and $(1-x)$Li$_2$SO$_4$–xAl$_2$O$_3$ [46] (**c**, **d**) on temperature and concentration of alumina. **b**, **d** Two curves for 0.33Li$_2$SO$_4$–0.67Al$_2$O$_3$ correspond to the samples prepared in different conditions

described by percolation model with two thresholds [95–98]. In the vicinity of these thresholds (at $f \sim 0.9$ and 0.1), the permittivity maxima are observed [69, 98, 99]. At temperatures where MX exists in molten or superionic states, the conductivity of the composites is lower than that of the individual salt and may be explained by a standard percolation model with one percolation threshold.

Most composite electrolytes reported in literature are submicrometric system with the effective grain size of 60–1000 nm. Transport properties of the nanocomposites with the grain size of order of 10 nm are less studied. Nevertheless, in these systems, true size effects are observed. For nanocomposites, there is a tendency to leveling conductivity parameters of the low- and high-temperature phases with the increase in the concentration of the oxide component. As a result, in $(1-x)$AgI–xAl$_2$O$_3$, the conductivities of the high-temperature (superionic) and low-temperature phases became equal, i.e., phase transition of the salt to the superionic state gradually disappears [74, 100] (Fig. 10a). The conductivity maximum ($\sim 10^{-3}$ S/cm at 25 °C) shifts to higher concentrations, 50–60 mol% (Fig. 10b). The activation energy in both superionic and low-temperature phases increased monotonically with x. On the temperature dependence of conductivity of the nanocomposite Li$_2$SO$_4$–Al$_2$O$_3$, there is no sharp conductivity jump at 575 °C associated with the transition of lithium sulfate to the superionic state (Fig. 10c) [46]. Instead, the $\sigma(T)$ dependence has a shape

Fig. 9 Phase diagram demonstrating the possibility of the spontaneous formation of the amorphous phase in the nanocomposites. As a result of the spreading, MX transforms first into the metastable crystalline state corresponding to the grains size of L''. Then this state relaxes into more stable amorphous state with larger particles; the increase in the effective particle size from L'' to L' may be due to the change of the particles shape
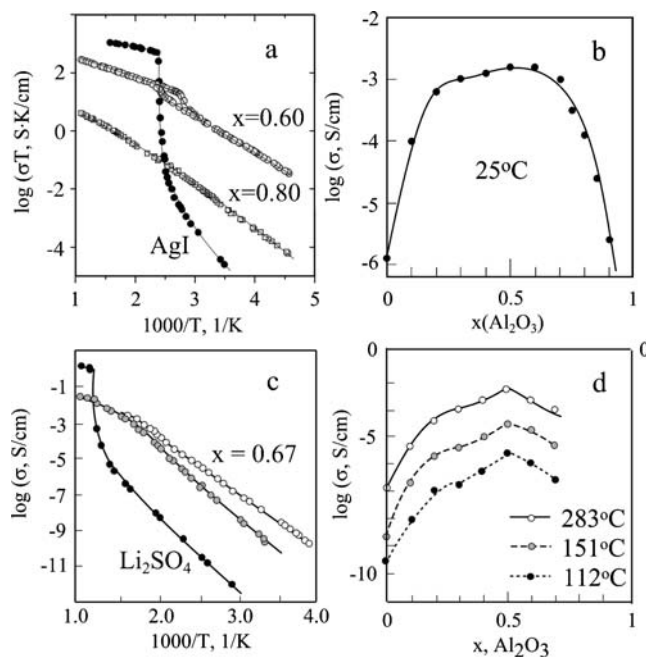
typical for solid electrolytes with the fluorite structure in the vicinity of the "diffuse" phase transition. Doping of alkali metal nitrates with highly dispersed alumina (S_A=270 m^2/g) is accompanied by a sharp increase in the conductivity (Fig. 11) [75, 76]. The conductivity of composites $(1-x)$ MNO$_3$–xAl$_2$O$_3$ (M = Li, Na, K, Rb, Cs) exhibits maxima at x=0.5–0.6; the relative increase (σ/σ_0) depends on the cation type and varies in the range from 10^2 (CsNO$_3$–Al$_2$O$_3$) to 10^8 at 343 K (in LiNO$_3$–Al$_2$O$_3$). For x>0.5–0.6, the Arrhenius plots of all composites are not linear and no conductivity jumps are observed. For example, for 0.4 RbNO$_3$–0.6Al$_2$O$_3$, the Arrhenius curve is a smooth line without four sharp jumps due to phase transitions (including melting) observed in pure rubidium nitrate [77]. It has been reported that nitrate-based composites are proton conductors in humid atmosphere [101]. We have studied in detail the transport properties of composites based on rubidium nitrate [76, 78]. The decomposition voltage, U_d=4 V, obtained by voltammetric measurements in vacuum was close to the corresponding values in fused alkali metal nitrates and halides. This makes it possible to assume that rubidium cations are the main mobile charge carriers in RbNO$_3$–Al$_2$O$_3$. Oxide additions in the composites CsCl–Al$_2$O$_3$ result in a gradual suppression of the abrupt conductivity change associated with the transition to the high-temperature polymorph, suggesting its stabilization at the interface [67]. In nanocomposites LiClO$_4$–Al$_2$O$_3$, no conductivity change is observed at the melting point of lithium perchlorate [40].

The conductivity data fairly correlate with results of calorimetric studies of the same systems. A change in the temperature, a decrease in the intensity, or a complete disappearance of the phase transitions is observed by both electrical measurements and DSC method. The strongest effects are observed only if the specific surface area of

Fig. 11 Temperature dependences of pure nitrates and the composites 0.5MNO$_3$–0.5Al$_2$O$_3$ with highly dispersed alumina (the specific surface area of S_A=270 m^2/g); M = Li, Na, K, Rb, Cs [75–77]

oxide additive is sufficiently high (S_A>~100 m^2/g), oxide particles are not packed into dense aggregates, and the components have high adhesion. Moreover, even in this case, one should provide conditions for effective spreading of the ionic salt MX on the oxide surfaces (thorough preliminary mixing followed by sintering). As a particular case, new metastable crystalline phases of AgI have been found in the AgI–Al$_2$O$_3$ composites. One of such phases, a 7H polytype of β-AgI [81, 102], cannot be prepared by any other method. Amorphous AgI may be obtained by fast cooling AgI – Al$_2$O$_3$ nanocomposites from 750 °C in liquid nitrogen [103]. Amorphous AgI also forms in the composites AgI–A (A = ZrO$_2$, CeO$_2$, Sm$_2$O$_3$, MoO$_3$, WO$_3$) obtained by the quenching technique [104]. Recently, it was shown that nanocomposites AgI–A (A = ZrO$_2$, Al$_2$O$_3$ xerogels and aerogels), where oxide additives had a high specific surface area of 150–500 m^2/g, exhibited unusual transport and thermodynamic properties [105, 106].

Conductivity of composite solid electrolytes

In contrast to ordinary composites of the insulator–conductor type where bulk conductivities prevail, in composite solid electrolytes, the ionic transport occurs mainly via interfaces; it complicates theoretical estimation of the transport properties in such systems. Theoretical calculations have been made on the basis of model estimations for specific morphologies [4, 8, 13, 26], simplified Maxwell–Garnett equation [107–109], the effective medium models [110–114], percolation theory, and computer simulations of several model systems [115–122].

A most accurate calculation of the conductivity in MX–A may be carried out for limiting cases ($f\rightarrow0$) and ($f\rightarrow1$) when the particles of A or MX are placed in the matrix of the second phase and are isolated from each other [26, 107–109]. Assuming that the dispersoid particles with a size L_A are isolated by the phase MX and are covered by conducting layers with the effective thickness λ, Jow and Wagner [26] derived an expression for the conductivity:

$$\sigma = \sigma_{MX} + 3 \times \sum_i e \times \upsilon_i \times \langle n_i \rangle \times \left(\frac{\lambda}{L_A}\right) \times \frac{f}{(1-f)},$$

(12)

where σ_{MX} is the bulk conductivity of MX; υ_i is the mobility of i-th defects; $\langle n_i \rangle$ is the mean arithmetic value between the defect concentrations in the bulk and on the interface; the summation is made over all mobile defects. This expression satisfactorily describes experimental data for CuCl–Al$_2$O$_3$, especially the conductivity dependence on the oxide grain size. However, it is only applicable for low

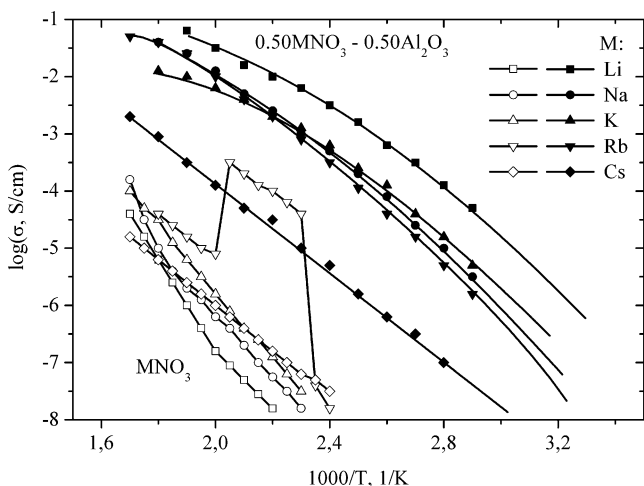concentrations of the oxide; at $f \rightarrow 1$, the conductivity should infinitely increase. Maier has proposed a more reasonable equation [4, 8, 13]:

$$\sigma = (1 - f)\sigma_{MX} + 3e\beta_L \times \frac{2\lambda_D}{L} \times f \times \upsilon \times \sqrt{n_\infty n_0}, \quad (13)$$

where β_L is the fraction of double layers participating in the conduction ($1/3 < \beta_L < 2/3$); λ_D is the Debye length; and n_∞ and n_0 are the defect concentrations in the MX bulk and at the interface, respectively. Using this equation and known defect mobility values, Maier quantitatively interpreted the data on conductivity in MX–Al$_2$O$_3$ (MX = AgCl, AgBr, TlCl) in the concentration range of $0 < f < 0.20$; the parameter β_L was taken as 0.5; the grains size of alumina was varied within the range of 0.06–0.3 μm. Equation 13 is in a better agreement with experiments, but cannot explain the conductivity maximum observed in all composites. In [107], the following expression was obtained on the basis of a simplified version of the Maxwell–Garnett equation:

$$\sigma = \left(\sigma_{MX} + \frac{3\lambda}{L_A} \times f \times \sigma_S\right) \times \frac{2 \times (1 - f)}{2 + f}, \quad (14)$$

where σ_S is the conductivity of MX in the interfacial layer of the thickness λ. This expression describes the conductivity maximum despite that the initial Maxwell–Garnett model is valid only for isolated particles, i.e., at low f values. Fujitsu et. al. [108, 109] have reported that this equation did not fit experimental data for SrCl$_2$–Al$_2$O$_3$, CaF$_2$–Al$_2$O$_3$, and CaF$_2$–Al$_2$O$_3$. The conductivity of model composites consisting of ordered isolated cubic particles A, covered by a conducting layer, has been calculated by Stoneham et. al. [110] and Wang and Dudney [111]; the authors varied the conductivity profile within the conducting layers and distance between the particles. The solutions have a complex analytical form, and the dependence of conductivity vs. concentration has a maximum depending on the conductivity and relative thickness of the conducting layer.

For the calculations in a whole concentration range, it was proposed to use the effective medium model [112–114]. Accordingly, the MX–A composite was modeled as a statistical mixture of spherical particles of MX and A with the same size. For conductivity of the composite (σ), the following expression was obtained [114]:

$$\left(\frac{f}{d}\right)^2 \times \frac{\sigma_A - \sigma}{\sigma_A + \left(\frac{z}{2} - 1\right) \times \sigma} + \left(1 - \frac{f}{d}\right)^2 \times \frac{\sigma_{MX} - \sigma}{\sigma_{MX} + \left(\frac{z}{2} - 1\right) \times \sigma} + 2 \times \left(\frac{f}{d}\right) \times \left(1 - \frac{f}{d}\right) \times \frac{\sigma_S - \sigma}{\sigma_S + \left(\frac{z}{2} - 1\right) \times \sigma} = 0 \quad (15)$$

where d is the packing density; σ_S is the conductivity along the MX–A interface; and z is the packing coordination number. The concentration dependences obtained from this equation have two percolation thresholds and a smooth maximum. Qualitatively similar dependences have been obtained elsewhere [112, 113]. In [115], the conductivity was estimated from probability of the current flow through a resistance network imitating the ensemble of the MX and A particles of the same size L arranged in a simple cubic lattice:

$$\sigma = \sigma_{MX} \times \left[\frac{8\lambda}{3L} \times \frac{n}{n_0} \times (1 - f)^3 \times f^2 + (1 - f)^2\right], \quad (16)$$

where λ is the thickness of the conducting layer and n and n_0 are the charge carrier concentrations in the conducting layer and in the bulk of MX, respectively. Equation 16 fairly fits the data on LiI–Al$_2$O$_3$ composites [1] with the conductivity maximum at 40 vol.% alumina. If the particle distribution is not uniform, the maximum shifts to higher f values. Results of computer simulations using the random resistor network model have been reported in [95–97, 118–120]; it was shown that the concentration dependence of the conductivity is described by the percolation equation with two thresholds: p_1 (insulator MX—composite ionic conductor) and p_2 (composite ionic conductor—insulator A); the values of p_1

and p_2 and the percolation exponents depend on the coordination number and dimensionality of the network [95, 119]. The dependences of conductivity on the grain size agree qualitatively with experimental observations. The drawback of these simulations is a lack of analytical expression appropriate for fast estimations. Nan and Smith [98] proposed a method for the quantitative calculation of the composite conductivity by dividing the whole concentration range into three regions separated by some characteristic concentrations:

$$f_1 = p_1 / (1 + \lambda/L_A)^3 \quad (17)$$

$$f_2 = 1 / (1 + \lambda/L_A)^3 \quad (18)$$

$$f_3 = 1 - p_1 + p_2 \times f_2. \quad (19)$$

The value of f_1 corresponds to the real percolation threshold which may differ from that for the theoretical value of $p_1 = 0.15$. At $f > f_1$, first infinite conducting cluster appears; at $f = f_2$, the infinite cluster envelopes the total volume of the composite and the conductivity reaches its maximum. The concentration f_3 corresponds to the percolation threshold from conducting to insulating state and also differs from the ideal value of $p_2 = 0.85$. At $f < f_1$ and $f > f_3$,

the conductivity is estimated using the Maxwell–Garnett equations. In the intermediate region $f_1 > f > f_3$, the effective medium model is employed with the parameters different for the cases $f < f_2$ and $f > f_2$. The obtained theoretical curves were reported to provide good quantitative description of the experimental data on Li_2SO_4–Al_2O_3 and LiCl–Al_2O_3 [98]. A similar model was applied by Sikerski and Prziluski [122] for interpretation of the conductivity data in polymer composite electrolytes containing oxide additives. In general, such model is rather complicated, as it includes four different equations. Moreover, there is an uncertainty in the determination of f_1, f_2, and f_3 values.

For description of the conductivity of composites of the 'conductor–insulator' type, a standard mixing equation was proposed [123, 124]:

$$\sigma^{\alpha} = (1 - f) \times \sigma_{MX}^{\alpha} + f \times \sigma_A^{\alpha}. \quad (20)$$

In traditional mixing rules, the parameter α is taken constant: $\alpha = 1$ and -1 for oriented composites consisting of parallel layers of the components when the conductivity is measured in parallel and perpendicular directions, respectively; $\alpha = 0$ and $1/3$ correspond to the Lichtenecker [125] and Landau–Lifshitz [126] equations, respectively. Analysis shows that the parameter α is determined by the composite morphology and may vary with the concentration. In [123, 124], it was assumed that α may be approximated by a linear dependence:

$$\alpha = (1 - f) \times \alpha 1 + f \times \alpha 2 \quad (21)$$

where $\alpha 1$ and $\alpha 2$ are determined by morphology of the composites in the dilute limits $f \rightarrow 0$ and $f \rightarrow 1$, respectively. The generalized mixing rule, Eq. 20, with the parameter α given by Eq. 21 provides a satisfactory description of the percolation-type behavior [123, 124].

For composite electrolytes, the mixing rule may also be rewritten in the following form:

$$\sigma^{\alpha} = (1 - f - f_S) \times \sigma_{MX}^{\alpha} + f_S \times \sigma_S^{\alpha} + f \times \sigma_A^{\alpha} \quad (f_S < f) \quad (22)$$

where f_S and σ_S are total concentration and the conductivity of interfacial regions, respectively; the parameter $\alpha(f)$ depends on the concentration in accordance with Eq. 21. Evidently, this equation reduces to Eq. 20 at $f_S \rightarrow 0$ or $\sigma_S \rightarrow 0$ when the contribution of interfaces to the total conductivity is negligible. Substituting f_S estimated from the brick wall model, Eq. 10, yields [124]:

$$\sigma^{\alpha(f)} = \left[1 - f - f(1 - f)2\beta \frac{\lambda}{L_A} \right] \times \sigma_{MX}^{\alpha(f)}$$
$$+ f(1 - f)2\beta \frac{\lambda}{L_A} \times \sigma_S^{\alpha(f)} + f \times \sigma_A^{\alpha(f)}. \quad (23)$$

The theoretical curves $\sigma(f)$ for a composite with $\sigma_{MX} = 1 \times 10^{-8}$ S/cm; $\sigma_A = 1 \times 10^{-10}$ S/cm; $\sigma_S = 1 \times 10^{-3}$ S/cm; $\beta = 3$; $\lambda/L = 0.1$ obtained for different $\alpha 1$ and $\alpha 2$ are presented in Fig. 12.

(a) $\alpha 1 > 0$, $\alpha 2 > 0$. The percolation threshold values p_1 and p_2 are close to 0 and 1, respectively. At low A concentration, the oxide particles are distributed around MX grains forming the conductive cluster even at $f \rightarrow 0$, whereas at high concentrations, each oxide particle is covered by thin MX layers. As a result, the percolation cluster exists practically in the whole concentration range and all composites have an enhanced conductivity.

(b) The case when $\alpha 1 > 0$, $\alpha 2 < 0$ is most typical. The first p_1 threshold is close to 0, whereas the position of p_2 depends on the $\alpha 1/\alpha 2$ ratio and corresponds to maximum of low-frequency dielectric permittivity. At
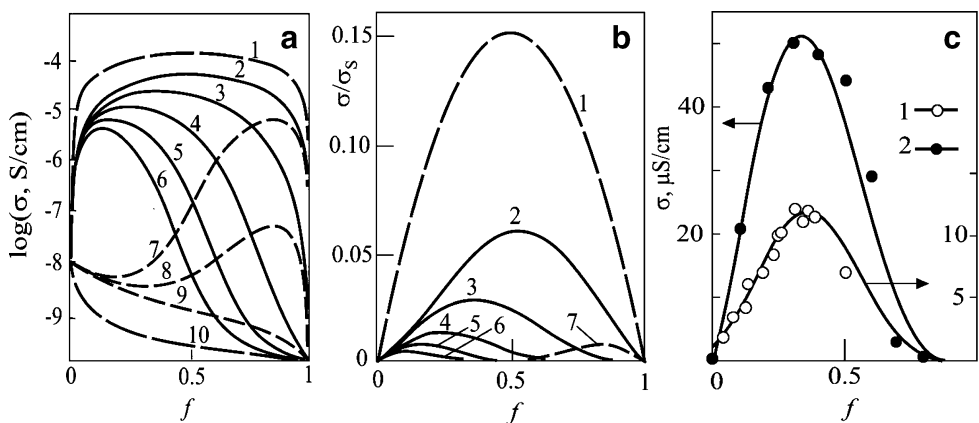

Fig. 12 **a**, **b** Theoretical curves s(f) for a composite with $\sigma_{MX} = 1 \times 10^{-8}$ S/cm; $\sigma_A = 1 \times 10^{-10}$ S/cm; $\sigma_S = 1 \times 10^{-3}$ S/cm; $\beta = 3$; $\lambda/L = 0.1$ obtained at different parameters $\alpha 1$ and $\alpha 2$ and represented in logarithmic (**a**) and linear (**b**) scale. Parameters ($\alpha 1$, $\alpha 2$) are equal to (1, 1), (3/2, 3/2), (3/2, 1/3), (3/2, 0), (3/2, −1/3), (3/2, −3/2), (−1/3, 2/ 3), (−1/3, 1/3), (−1/3, 0), and (−1, 1) for curves 1, 2, 3, 4, 5, 6, 7, 8, 9, and 10, respectively. (**c**) Comparison of experimental conductivity data for composites LiI–Al_2O_3 [1] and AgCl–Al_2O_3 [99] (symbols 1 and 2, respectively) with theoretical curves, Eq. 23

$f = p_2^* = \alpha 1/(\alpha 1 - \alpha 2)$, there is an inflection point where the maximum conductivity change is observed in logarithmic scale. This point is higher than the percolation threshold p_2 and may be called a "logarithmic" percolation threshold: at $f < p_2^*$, the composite behaves like a conductor, whereas at $f < p_2^*$ as a typical dielectric. At $\alpha 1 > 0$, the curve $\sigma(f)$ has a maximum; its position is determined by $\alpha 1$ and $\alpha 2$. For random mixtures, it was shown that $\alpha 1 < 2/3$; $\alpha 2 > -1/3$ [30]. The real composites cannot be considered as statistical mixtures since the A particles at low concentrations are not distributed uniformly but located along MX grains. This leads to an increase in $\alpha 1$ values up to 1.
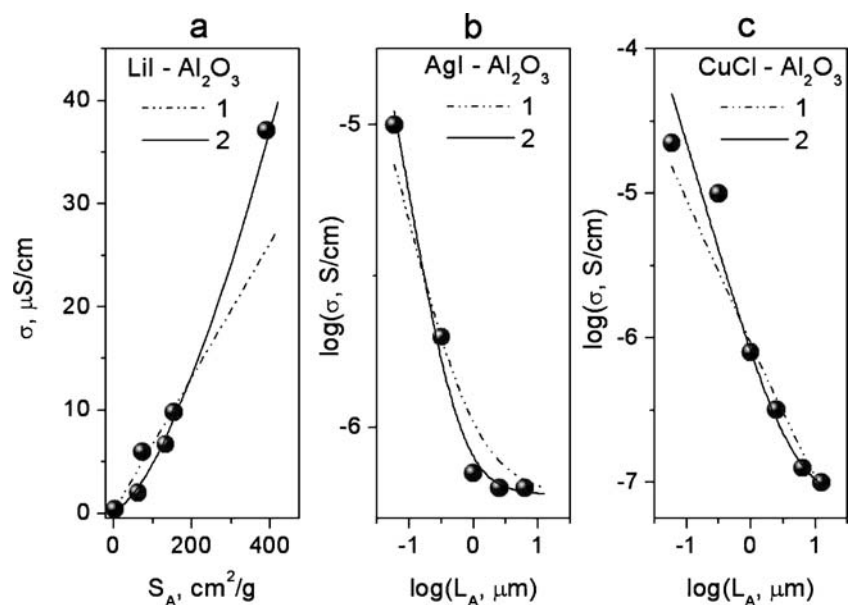
(c) $\alpha 1 < 0$, $\alpha 2 > 0$; $|\alpha 1| < |\alpha 2|$. In this case, at low f, the conductivity decreases. At higher concentrations, the conduction increases with f and goes through a maximum at $0.8 < f < 1$. In practice, no such composites are known.

(d) $\alpha 1 < 0$, $\alpha 2 < 0$. In this case, no conductivity enhancement may be observed.

The theoretical curves, Eq. 23, fit well experimental data for the systems LiI–Al$_2$O$_3$ [1] and AgCl–Al$_2$O$_3$ [99] (Fig. 12); they are in a qualitative agreement with effective medium model and percolation theory [110–122]. The generalized mixing rule, Eq. 23, with four fitting parameters [$\alpha 1$, $\alpha 2$, (λ/L) and σ_S] may be used for description of the experimental data.

In the case of $(2\beta\lambda/L) \times \sigma_S \gg \sigma_{MX}$, σ_A Eq. 23 reduces to the form:

$$\sigma \approx \sigma_S \times \left[f(1-f)2\beta \frac{\lambda}{L_A} \right]^{\frac{1}{\alpha 1 \times (1-f) + \alpha 2 \times f}}, \qquad (24)$$

which is suitable for approximate analysis of the dependences of conductivity on concentration and grain size. According to the theoretical models reported earlier [4, 8, 13, 26, 107–109, 110–114], the conductivity should increase inversely to the grain size, $\sigma \sim L_A^{-1}$, or proportionally to the specific surface area, $\sigma \sim S_A$ [which may be estimated as $S_A \approx 3 \cdot (\rho_A \cdot L_A)^{-1}$, where ρ_A is the oxide density]. This conclusion follows from Eqs. 12, 13, 14, and 15. The experimental dependences $\sigma(S_A)$ and $\sigma(L_A^{-1})$ obtained for LiI–Al$_2$O$_3$ [127], AgI–Al$_2$O$_3$, and CuCl–Al$_2$O$_3$ [128] with different grain size are shown in Fig. 13. From Eq. 24, it follows that the conductivity dependences on the grain size or the specific surface should be described by power functions $\sigma \sim L_A^{-1/\alpha}$ and $\sigma \sim S_A^{1/\alpha}$ [where the exponent $\alpha(f)$ is determined by parameters $\alpha 1$, $\alpha 2$, f: $\alpha = \alpha 1 \times (1-f) + \alpha 2 \times f$] rather than a linear function. The power dependences $\sigma = \sigma_0 + A \times S_A^{1/\alpha}$ and $\sigma = \sigma_0 + A \times L_A^{-1/\alpha}$ with an exponent of $\alpha = 0.67 \pm 0.1$ fit the experimental data with smaller deviations than linear models ($\alpha = 1$). Substituting typical values of $\alpha 1 \approx 1$, $\alpha 2 \approx 0$, and $f \approx 0.3$–0.4 to Eq. 21, one can obtain $\alpha \approx 0.6$–0.7 that is in agreement with the experiment. As follows from Eq. 24, linear dependences $\sigma \sim S_A$ or $\sigma \sim L_A^{-1}$ could be observed only in the limit $f \to 0$ at $\alpha 1 \approx 1$ or for a special morphology of the composites, e.g., when MX and A layers are oriented in parallel to the direction of the electric field direction and $\alpha 1 = \alpha 2 = 1$. In general, the conductivity should obey the power function with the exponent higher than unity.

All the equations mentioned above are valid until the surface conductivity, σ_S, does not depend on the effective size of MX crystals. However, generally, one should take into account the $\sigma(L)$ dependence, i.e., the size effect for the conductivity. Analytical forms of such dependence have

Fig. 13 Experimental values of conductivity of composites LiI–Al$_2$O$_3$ [127], AgI–Al$_2$O$_3$, and CuCl–Al$_2$O$_3$ [128] with different grains size of alumina fitted to linear ($\sigma = \sigma_0 + A_1 \times S_A$ and $\sigma = \sigma_0 + A_2 \times L_A$) and power ($\sigma = \sigma_0 + A_3 \times S_A^{1/\alpha}$ and $\sigma = \sigma_0 + A_4 \times L_A^{1/\alpha}$) dependences (curves 1 and 2, respectively)

been obtained by Maier [13, 129] and Khaneft [130] for pure nanocrystal under assumption that the concentration, mobility of the defects on the surface, and the defect formation energy in the bulk are constant. According to theoretical estimations, the defect formation energy decreases on scaling down of the grains size [131, 132]. The Debye length, being a function of the defect concentration, should also diminish. The ion mobility may also change with L. All these effects make it difficult to calculate the conductivity variations vs. grains size. Moreover, at high concentration of defects, phase transitions into the disordered states may occur on the surface [133] or in the bulk [134–136]. In nanocomposites, the situation may be still more complicated. Nevertheless, most experimental data may be satisfactorily interpreted under the assumption that the conductivity occurs in the interface disordered phase comprising a layer of the constant thickness λ, which is characterized by a high defect concentration.

Molecular dynamics simulations

Computer simulations provide means to understand the atomic mechanisms and to model local structure near interfaces on a microscopic scale. In spite of great progress in applying molecular dynamics (MD) simulations in solid state science [137], there have been practically no papers dealing with modeling of the interface between an ionic salt and an oxide, except for the recent papers on LiI–Al$_2$O$_3$ [138], CsCl–Al$_2$O$_3$ [139], and CaF$_2$–BaF$_2$ [140] nanocomposites. In [138], an oriented nanocrystal of LiI with a thickness of 100 monolayers was placed between the surfaces of two crystals of α- or γ-alumina. The hybrid

model potential function including a sum of a two-body and a three-body potentials was used for MD simulations. The two-body potential consisted of a Coulomb interaction, exponential repulsion, modified Born–Mayer, dispersive, quadrupole–dipole, and a Born repulsive term. The three-body potential included only the Al–O nearest neighbor interactions. The simulations showed that the conductivity of LiI increased when it was mixed with both α- and γ-alumina. Lithium ions adsorb on vacant tetrahedral sites of the alumina surface, leaving cation vacancies under the interface. This effect is more pronounced for α-alumina and less expressed for the γ-alumina surface. The diffusion coefficient, D_{Li}, was higher for the LiI–α-Al$_2$O$_3$ composites, though the activation energies were similar in both cases. These results agree with the model of chemical adsorption [4].

In [139], MD simulations of CsCl–α-Al$_2$O$_3$ using the two-layer model were reported. CsCl was placed in contact with alumina, heated up to 1,100 K, and transformed in the molten state. A nanocomposite was obtained after steep cooling down to 400 K, followed by crystallization of the salt. The interface was stable only for special relative orientations of crystal lattices of the contacting phases. For example, if the ($10\bar{1}0$) plane of alumina and (100) plane of CsCl contacted, a strong repulsion resulted in plastic deformation and long-term reconstruction of the interface. In order to make the system able to form energetically favorable orientation of crystal structure spontaneously, we simulated crystallization from the melt. The system after crystallization is shown in Fig. 14a. One can see that the crystal planes (110) of CsCl are slightly inclined against the alumina plane due to the lattices misfit. The ionic salt represents a single crystal which consists of two domains disoriented by 3–3.5° in two perpendicular (110) planes and

Fig. 14 **a** Equilibrium structure of CsCl–α-Al$_2$O$_3$ nanocomposite after recrystallization simulated by MD. **b** Trajectories of the most mobile ions recorded during 10^{-10} s
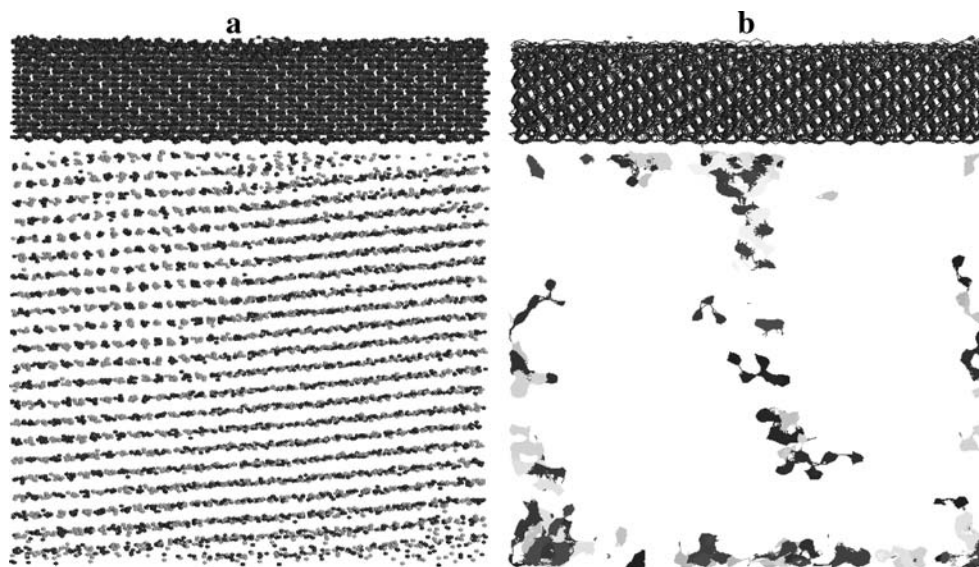
separated by a small-angle boundary. This boundary is generated by interface misfit dislocations and seems to join those located on two opposite CsCl–Al$_2$O$_3$ interfaces. The structure of alumina also undergoes changes; however, these changes are not so strong as in CsCl. The dislocation core is clouded by many defects, forming a region with an increased ion mobility. Also, incoherent grain boundaries are a source of free volume in the lattice and may hence act as migration paths. Figure 14b shows the trajectories of the most mobile ions recorded during 10^{-10} s. One can see that most mobile ions are concentrated near the interface in a core of the misfit dislocation and also in the vicinity of interdomain boundary, located in the bulk of cesium chloride and formed during crystallization. The diffusion coefficients of mobile cesium and chloride ions are close to each other, nearly ~10^{-6} cm^2/s at 700 K, i.e., are an order of magnitude lower than those in molten alkali halides [141].

Recently [140], layered composites comprising parallel stacked arrays of two crystalline fluoride conductors, CaF$_2$ and BaF$_2$, have been modeled by MD. The CaF$_2$ regions in the layered system were compressed along the c-axis perpendicular to the interface. On the other hand, the BaF$_2$ regions were stretched along the c-axis. The diffusion coefficient and the ionic conductivity of F$^-$ ions increased with decreasing periods in the layered fluoride conductors. Although these results agree with experiment [142, 143], the authors mentioned that they had to fix the lattice constant at the interface to provide the stacking coherency and stability; otherwise, the heterostructure would be unstable due to great misfit between the crystal lattices.

The results of MD simulations unambiguously show that the ion diffusion in the composites is faster than in pure salts. However, there are several possible reasons of this effect:

(a) ion adsorption at the oxide surface with the formation of space charge layer, enriched in defects;
(b) lattice deformation near the interface resulting in changing free volume; and
(c) the appearance of domains and low-angle interdomain boundaries generated by the misfit dislocations. The ions located near the boundaries have an enhanced mobility.

Mechanism (a) seems to be typical for strong interface interaction and small misfit between the lattices MX and A when the adsorption of ions takes place with the formation of a space charge. The second mechanism relates to the case of weak interfacial interaction (without ion adsorption) and relatively large lattice misfit leading to the lattice deformation. The third mechanism may be similar to (a) and (b); however, in this case, the misfit is so high that the coherent interfaces become unstable and the misfit dislocations form on the surface. Thus, besides "pure" chemical adsorption, there are additional factors typical for solid state systems, such as a misfit of the crystal lattices (given by the orientation of crystallographic planes) and mechanical properties of the components (determining the deformation, type, and concentration of dislocations and domain boundaries).

Design of composites and new types of composite solid electrolytes

### Variation of the chemical nature of MX and A pair

This approach is traditional and may be useful for the comparative analysis of the interfacial effects in a series of composites. To obtain composites with improved properties, one could vary ionic salt or oxides provided that no chemical interaction takes place between the components and oxide particles are kinetically stable in the operating temperature range of the composite. The same approach is also used for optimization of properties of composite materials intended for applications in particular operation conditions. It was shown [25] that lithium salts in systems with alumina exhibit a stronger increase in conductivity as compared to rubidium and cesium salts, while iodides more readily form nanocomposites as compared with chlorides and fluorides. This suggests that the polarizing effect of the cation and the polarizability of the anion in the ionic component play an important role in the surface interaction mechanism. The physical reason for the surface interaction in a composite of the ionic salt-oxide type originates from the tendency of both substances to decrease their surface energy due to the interaction of surface ions with the ions of neighboring phase. Owing to the difference in inter-ionic energies and peculiarities of the crystal structures in the interfacial layers, the ideal structure inherent in individual phases will be distorted in such a way as to provide a gain in the surface energy due to the mutual approachment or removal of surface atoms. The relative displacement of ions from their ideal positions is determined by the balance of the interaction energies. Insofar, as in alumina, for the majority of discussed MX salts, anions exceed cations in size; it can be expected that for close packing, the interface cations will have the larger free volumes and will be displaced for longer distances than the anions. As a result, in the space between the surface layers, an intermediate positively charged layer enriched with cations is formed; its charge is compensated by the cationic vacancies that constitute the diffuse layer. This process may be regarded as a chemical adsorption [4, 13] and can be presented as the following quasi-chemical reaction:

$$0 \leftrightharpoons V'_M + (M - A)^{\cdot}_S \qquad (25)$$

which describes the stage of the surface disordering of MX at the MX–A interface. If an anion is adsorbed on the surface, another reaction proceeds:

$$0 \rightleftharpoons V_X^{\cdot} + (X - A)_S^{'}. \tag{26}$$

The isoelectric point of an oxide pE was proposed [144] as a measure of its surface activity. Indeed, equations similar to Eqs. 25 and 26 may be written for the surface interaction of an oxide with water:

$$H_2O \rightleftharpoons OH' + (H - A)_S^{\cdot} \tag{27}$$

$$2H_2O \rightleftharpoons H_3O^{\cdot} + (OH - A)_S^{'}. \tag{28}$$
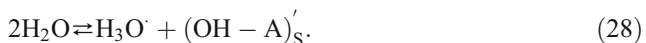
The first reaction predominates for oxides with $pE>7$, for instance MgO, Al_2O_3, CeO_2; the second prevails for the oxides with $pE<7$ (ZrO_2, SiO_2). By analogy with aqueous solutions, one can expect that the surface reaction 25 should occur in composites containing basic oxides ($pE>7$), whereas for acidic oxides ($pE<7$), the interface interaction should follow the mechanism 26. The isoelectric point of any oxide changes due to its doping with different species or by direct modification of its surface by acidic or basic agents. It enables to increase the conductivity of the composite only by the variation of its surface properties. A more general approach is to change Lewis acidity/basicity of the oxide surface. Both approaches were successfully used for the improvement of transport properties of different composites [39]. Unfortunately, insufficient amount of experimental data to date makes it difficult to check correctness of the direct transfer of the model of acid–base equilibria in aqueous solutions. The conductivity enhancement in composites containing ferroelectric oxides $BaTiO_3$, $LiNbO_3$, and $KTaO_3$ is reported [145–147]. The effect was proposed to be strengthened due to high dielectric permittivity of the oxide.

Change of the physical state of ionic salt in MX–A composites

One serious problem of crystalline composite solid electrolytes is a poor contact between the crystallites of MX and A, leading to the formation of porous and brittle ceramics. To avoid this problem, liquid, glassy, or polymer electrolytes may be used instead of crystalline ones. Among the composites of this type, the systems based on polymer or gel electrolytes are most extensively studied. They comprise solutions of ionic salts in liquids or polymers mixed with dispersed oxide fillers, such as oxides, nitrides, zeolites, ferroelectric oxides, lithium compounds, etc. [148–161]. Due to the filler presence, the composite not only maintains its mechanical stability but also has an increased conductivity. It was demonstrated that the conductivity enhancement depends on the chemical properties of

dispersed ceramics and its morphology [149, 152]. The main reason for this effect seems related to the stabilization of amorphous phase, i.e., to a suppressed formation of crystalline phases with much lower ionic conductivity. This occurs owing to the surface groups of ceramic particles promoting local transformation from crystalline to amorphous state where the mobility of ions is higher [153, 154]. Another reason for the conductivity enhancement is an easier dissociation of the ionic salt in the vicinity of interface [151–161]. The latter effect is observed even at high temperatures where polymer is in a liquid state and is accompanied by an increase in the cation transference number t^+ [149, 150] important for the applications in lithium batteries [149–152]. In (PEO–LiClO$_4$)–Al$_2$O$_3$ composites, the conductivity and t^+ both increase when introducing, sequentially, basic, neutral, and acidic Al$_2$O$_3$ additions [150]. Hence, it is not surprising that no conductivity enhancement was observed in some systems [154]. The MX–A composites with inorganic glassy solid electrolytes MX were reported [162, 163]. As mentioned in Section 4, the amorphous non-autonomous phases form in nanocomposites MX–A (MX = AgI, MeNO$_3$, LiClO$_4$, CsHSO$_4$; Me is alkali cation; A is highly dispersed or porous Al$_2$O$_3$, SiO$_2$) [14, 17, 25, 40, 41, 46, 48, 49, 67–69, 74–80, 82, 83, 100, 103, 104]. These systems may be formally considered to the composites with glassy electrolytes. Solid solutions or mixtures of two salts were also suggested as solid electrolytes in MX–A systems. The composites of the (MX–MX′)–A type exhibit, in general, higher conductivities in comparison with pure MX–MX′ systems [164–166].

Change of the physical state of inert non-conducting component

Instead of the solid oxide filler A in MX–A systems, one can use polymer network or glassy phase, either impregnated with a ion-conducting liquid phase or containing crystalline component MX. Typical examples of such systems are polymer proton-conducting membranes containing end acidic groups and easily absorbing water, e.g., NAFION-type materials. At sufficiently high concentrations of the absorbed water, a network of liquid phase channels provides high proton transport [167–169]. A qualitatively similar conductivity mechanism occurs in the gel electrolytes [170], ion exchange membranes, clays, and zeolites [171]. The polymer membranes are characterized by poor mechanical stability which may be improved by reinforcement by rigid support or solid fillers. Solid electrolytes MX–A with amorphous additive possessing a high mechanical strength may be obtained in systems of the 'ionic salt–glass' type. The most known systems of the latter type are composite electrolytes with amorphous silica MX–SiO$_2$ (MX = LiI [172], LiBr [173], LiCl [6], AgI [5,

10], AgCl [4], RbNO$_3$ [78]) which have high ionic conductivity. As silica is the chemical stable towards acids, it may be used in composite solid electrolytes with solid acids, e.g., MHSO$_4$–SiO$_2$ (M = Cs, Rb) [48, 49, 79], CsH$_2$PO$_4$–SiO$_2$ [174], CsH$_2$PO$_4$–SiP$_2$O$_7$ [175], and Cs$_3$H$_5$(SO$_4$)$_2$–SiO$_2$ [176]. These and other composites of the latter type have a high proton conductivity and are promising solid electrolytes for fuel cells [175, 177–179]. AgI–glass composites were obtained by controlled crystallization of AgI from supersaturated glass compositions [180–183]; the composites contained nanoparticles of the frozen-in high-temperature α-AgI polymorph and exhibited a fast ionic conduction [180–182]. Recently, the composites containing Li$_2$S in sulfide or oxy-sulfide glasses were shown to display a high lithium-ion conductivity [184, 185] which may be used in lithium solid-state batteries [186].

Modification of the morphology of inert component (geometric aspect)

The term 'morphology' (or its equivalents: micro- and mesostructure) involves all geometric parameters of the system: shape, dimension, and relative arrangement of all elements of the system, including the grains, pores, and interfaces. The conductivity of composites may be controlled in a wide range by variation of the morphology even without changing the effective grain (or pore) size. For this purpose, one can use oxide additives with particles of different dimensionality, taking into account that for one-dimensional (wires, fibers, tubes, rods) or two-dimensional (layers, sheets, plates, foams) systems, the orientation of individual particles has a strong effect on macro properties of the composite. There are practically no literature data on the influence of morphology on the conductivity of composite electrolytes. Dudney [187] has studied AgCl–Al$_2$O$_3$ composites with alumina fibers as a filler. There is an increasing interest in the artificial micro- and nano-heterostructures prepared in situ using a controlled procedure that allows making of the preset architecture [24, 188]; an example of such systems is the multilayered heterostructure comprising an array of alternating layers of two ionic salts CaF$_2$–BaF$_2$ prepared by the molecular beam epitaxy [142, 143]. Such structures possess high ionic conductivity depending on the thickness of the unit layer and on the heterostructure orientation. Other examples are the oxide and hydroxide layers obtained by the successive ionic layer deposition technique [189].

## Preparation of the metacomposite materials and nanostructured systems

In all the cases mentioned above, physical and chemical properties of inert oxide additive do not change. Another situation is observed in metacomposites, i.e., heterogeneous systems with the interfacial interaction changing physico-chemical properties of both components [190, 191]. Moreover, such a heterosystem exhibits properties which are not typical for both individual components. These materials constitute a new interesting class of metamaterials. The structured or nanostructured composite materials with oriented grains and coherent interfaces may be obtained also on the spinodal decomposition of solid solutions with NaCl-type structure [192, 193] or perovskite-related systems [194–196]. They exhibit, again, an enhanced ionic conductivity at low temperatures caused by the interfacial phenomena.

Scaling of the systems down to a nanoscale level

This is one of the most effective approaches to develop new materials with advanced characteristics. To prepare such systems, one has to use inert nanodispersed or nanoporous fillers or matrices not interacting chemically with ionic components. The stability of the nanocomposites is determined by the adhesion energy between the components, as discussed in Section 3. The mechanism of the adhesion includes the same quasichemical reactions (25 and 26) that take place in ordinary composites, but the impact of the interface interaction is much stronger. In Section 4, the discussed nanocomposites are usually prepared using highly dispersed oxides with the characteristic size of grains or pores of ~10 nm. In these systems, strong size effects were observed and new interface-stabilized non-autonomous highly conducting phases were found. Mesoporous oxides with ordered arrangement of pores are the promising matrixes for the development of new composite electrolytes. Particles of such oxides contain pores of identical diameter which are long-range ordered and form one-, two-, or three-dimensional superstructures, with the lattice parameter varied from 3 to 16 nm [197, 198]. Recently, an enhanced ionic conductivity was reported for nanocomposites of the MX–A type, LiI–A (A = Al$_2$O$_3$, SiO$_2$) [199–201], polymer composite electrolytes, (polymer–LiX)–A, where (polymer–LiX) is the solution of the lithium salt in polymer (X = ClO$_4^-$, SO$_3$F$^-$) [202–205] or mesoporous proton-conducting membranes [206] with mesoporous oxide additives. Figure 15 shows the dependences of conductivity of nanocomposites $(1-x)$LiClO$_4$–xSiO$_2$ on temperature and on the concentration of additives, including the mesoporous silica and MCM-41 [207]. The sample was obtained by the impregnation of lithium salt into the mesoporous matrix. The composite with $x > 0.5$ exhibits a high conductivity and a complete absence of the conductivity jump at the melting point. This suggests that the ionic salt is in the amorphous state. In general, taking into consideration a great progress achieved during the last years in the

Fig. 15 High-resolution electron microscopy pattern of LiClO$_4$–SiO$_2$ nanocomposite with mesoporous silica MCM-41 at $x=0.6$ (**a**). Arrhenius dependences of the conductivity of these composites at different molar concentrations of the oxide (**b**)
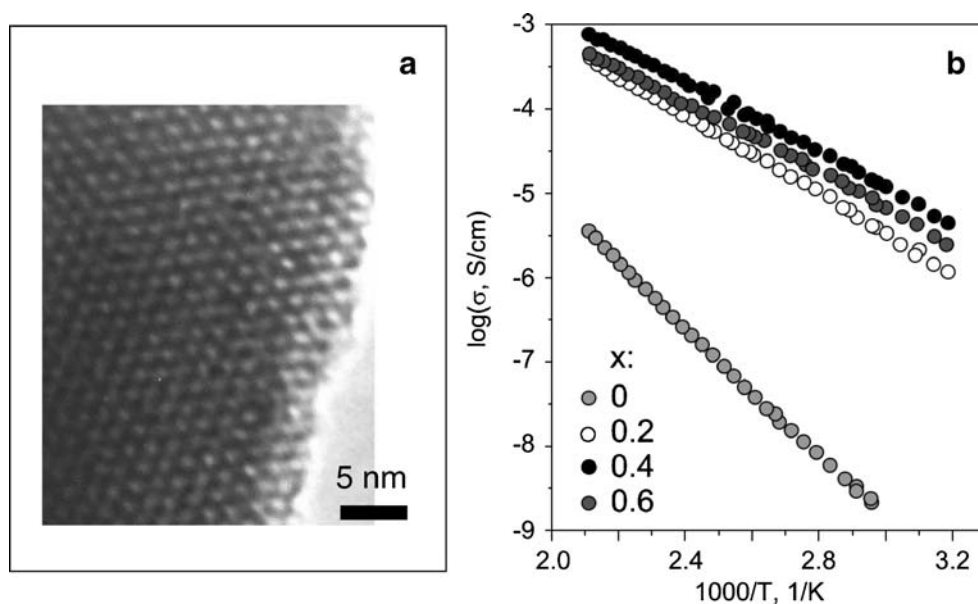
development of nanosystems with specific morphologies [208], the nanocomposites of new types are expected to be created in the near future. It should be mentioned that there is an optimal size of grains or pores of the oxide when the conductivity enhancement effect is maximal. On further decrease in size, the nanocomposites cannot form. This fact was first observed by Ponomareva et. al. [48, 49] and confirmed in subsequent works [201, 209]. The effect may be explained by the contribution of strains energy; its thermodynamic origins are discussed in Section 3.

All the approaches mentioned may be constructively combined in order to obtain the composites and nanocomposite electrolytes with a high performance and adopt them for particular applications in batteries, fuel cells, supercapacitors, sensors, and other electrochemical devices.

Conclusion

The physical properties of composite solid electrolytes were briefly reviewed with emphasis on the interfacial interaction between the components and the impact of interfaces on the thermodynamic and transport properties. The surface potential formation and the point defects equilibrium at free surfaces and interfaces were considered in frame of the Stern model, which provides a common basis for quantitative description of the surface and interface effects. Special attention was focused on the size effects, i.e., changes in the bulk characteristics of ionic salts in nanocomposites due to the influence of interface energy and to the formation of the interface phases. The main thermodynamic reason for the formation of nanocomposites as well as for the stabilization of non-autonomous interface phases is the adhesion energy,

γ_a. At sufficiently high γ_a, values the ionic salt tends to spread along the oxide surface. If the grain size of the oxide is sufficiently small, the nanocomposite forms upon sintering. The adhesion results from the interface interaction and comprises the stage of specific adsorption of the interface ions. This leads to forming double layer in the interfacial region of ionic salt. In the case of strong adhesion, structural reconstruction or formation of the interface phases may occur. Analysis of the experimental data revealed that interface phases exist in composites AgI–Al$_2$O$_3$, MeNO$_3$–Al$_2$O$_3$ (Me = Li, Na, K, Rb and Cs), CsHSO$_4$–SiO$_2$, RbNO$_3$–SiO$_2$, and CsCl–Al$_2$O$_3$. Their structure may be either epitaxial crystalline, or amorphous. The thickness of the interface phase estimated on the basis of the brick wall model is about 3–4 nm. The reason for stabilization of non-equilibrium states is complex and translates the influence of several factors, namely, the interfacial interaction between the components, particle size effect, and elastic strains in the lattice of ionic salt. The results of MD simulations showed that the main mechanisms of the conductivity enhancement are the adsorption of ions to the oxide surface with formation of space charge layer, the lattice deformation near the interface, and the appearance of domains and low-angle interdomain boundaries generated by the misfit dislocations. All the above mechanisms are induced by the interfaces. The equations proposed earlier for the description of the conductivity of composites were analyzed. Among them, the general mixing rule has a rather simple analytical form and provides appropriate description of the experimental conductivity data for the composite solid electrolytes in a whole concentration range. Main approaches for the improvement or creating new composite systems were analyzed.

References

1. Liang CC (1973) J Electrochem Soc 120:1289. doi:10.1149/1.2403248
2. Shahi K, Wagner JB (1981) Solid State Ion 3/4:295. doi:10.1016/0167-2738(81)90101-6
3. Wagner JB (1985) Composite materials as solid electrolytes. In: Sequeira CAC, Hooper A (eds) Solid state batteries. Matinus Nijhoff, Dordrecht, p 77
4. Maier J (1985) J Phys Chem Solids 46:309. doi:10.1016/0022-3697(85)90172-6
5. Khandkar AC, Wagner JB (1986) Solid State Ion 18/19:1100. doi:10.1016/0167-2738(86)90316-4
6. Chen L (1986) Composite solid electrolytes. In: Chowdhari BVR, Radhakrishna S (eds) Materials for solid state batteries. World Science Publishing, Singapore, p 69
7. Shukla AK, Vaidehi N, Jacob KT (1986) Proc Indiana Acad Sci 96:533. doi:10.1007/BF02936304 (Chem Sci)
8. Maier J (1987) J Electrochem Soc 134:1524. doi:10.1149/1.2100703
9. Maier J (1989) Heterogeneous solid electrolytes. In: Chandra S, Laskar A (eds) Superionic solids and solid electrolytes: recent trends. Academic, New York, p 137
10. Wagner JB (1989) Composite solid electrolytes. In: Takahashi T (ed) High conductivity conductors: solid ionic conductors. World Science Publishing, Singapore, p 102
11. Dudney NJ (1989) Annu Rev Mater Sci 19:103
12. Uvarov NF, Isupov VP, Sharma V, Shukla AK (1992) Solid State Ion 51:41. doi:10.1016/0167-2738(92)90342-M
13. Maier J (1995) Prog Solid State Chem 23:171. doi:10.1016/0079-6786(95)00004-E
14. Uvarov NF (1996) Unusual bulk properties of ionic conductors in nanocomposites. In: Chowdary BVR et al (ed) Solid state ionics: new developments. World Science Publishing, Singapore, p 311
15. Agrawal RC, Gupta RK (1999) J Mater Sci 34:1131. doi:10.1023/A:1004598902146
16. Yarostalvtsev AB (2000) Russ J Inorg Chem 45(Suppl 3):249
17. Uvarov NF, Vanek P (2000) J Mater Synth Process 8:319. doi:10.1023/A:1011346528527
18. Maier J (2002) Solid State Ion 154–155:291. doi:10.1016/S0167-2738(02)00499-X
19. Maier J (2003) Solid State Ion 157:327. doi:10.1016/S0167-2738(02)00229-1
20. Jamnik J, Maier J (2003) J Phys Chem Chem Phys 5:5215. doi:10.1039/b309130a
21. Heitjans P, Indris S (2003) J Phys Condens Matter 15:R1257. doi:10.1088/0953-8984/15/30/202
22. Maier J (2004) Solid State Ion 175:7. doi:10.1016/j.ssi.2004.09.051
23. Schoonman J (2000) Solid State Ion 135–137:5. doi:10.1016/S0167-2738(00)00324-6
24. Maier J (2005) Nat Mater 4:805. doi:10.1038/nmat1513
25. Uvarov NF (2007) Russ Chem Rev 76:415. doi:10.1070/RC2007v076n05ABEH003687
26. Jow T, Wagner JB (1979) J Electrochem Soc 126:1963. doi:10.1149/1.2128835
27. Stern O (1924) Z Electrochem 30:508
28. Uvarov NF (2007) Russ J Electrochem 43:368. doi:10.1134/S1023193507040027
29. Uvarov NF (2008) Solid State Ion 179:783. doi:10.1016/j.ssi.2008.01.043
30. Frenkel J (1946) Kinetic theory of liquids. Oxford University Press, Oxford
31. Kliewer KL, Koehler KS (1965) Phys Rev A 140:1226
32. Kliewer KL (1966) J Phys Chem Solids 27:705. doi:10.1016/0022-3697(66)90221-6
33. Poeppel RB, Blakely JM (1969) Surf Sci 15:507. doi:10.1016/0039-6028(69)90138-1
34. Jamnik J, Maier J, Pejovnik S (1995) Solid State Ion 75:51. doi:10.1016/0167-2738(94)00184-T
35. Heyne L (1983) Interfacial effects in mass. Transport in ionic solids. In: Beniere F, Catlow CRA (eds) Mass transport in solids. Plenum, New York, p 425
36. Guo X, Maier J (2001) J Electrochem Soc 148:E121. doi:10.1149/1.1348267
37. Guo X, Waser R (2006) Prog Mater Sci 51:151. doi:10.1016/j.pmatsci.2005.07.001
38. Lauer U, Maier J (1990) Sensors Actuators B 2:125. doi:10.1016/0925-4005(90)80021-Q
39. Saito Y, Maier J (1995) J Electrochem Soc 142:3078. doi:10.1149/1.2048691
40. Ulihin AS, Uvarov NF, Mateyshina YG, Brezhneva LI, Matvienko AA (2006) Solid State Ion 177:2787. doi:10.1016/j.ssi.2006.03.018
41. Ulihin AS, Slobodyuk AB, Uvarov NF, Kharlamova OA, Isupov VP, Kavun VY (2008) Solid State Ion 179:1740. doi:10.1016/j.ssi.2008.02.027
42. Gurevich YY, Pleskov YV (1983) Photoelectrochemistry of semiconductors. Nauka, Moscow, p 62
43. Sato N (1998) Electrochemistry at metal and semiconductor electrodes. Elsevier, Amsterdam, p 127
44. Maier J (1985) Ber Bunsenges Phys Chem 89:355
45. Adamson AW, Gast AP (1997) Physical chemistry of surfaces. Wiley, New York, p 108
46. Uvarov NF, Bokhonov BB, Isupov VP, Hairetdinov EF (1994) Solid State Ion 74:15. doi:10.1016/0167-2738(94)90432-4
47. Uvarov NF, Boldyrev VV (2001) Russ Chem Rev 70:265. doi:10.1070/RC2001v070n04ABEH000638
48. Ponomareva VG, Lavrova GV, Simonova LG (1999) Solid State Ion 118:317. doi:10.1016/S0167-2738(98)00429-9
49. Ponomareva VG, Lavrova GV, Simonova LG (2000) Solid State Ion 136–137:1279. doi:10.1016/S0167-2738(00)00589-0
50. Maier J (2003) Z Phys Chem 217:415. doi:10.1524/zpch.217.4.415.20385
51. Komnik YF (1979) The physics of metallic films. Size and structural effects. Atomizdat, Moscow, p 62
52. Nepiiko SA (1985) Physical properties of small metallic particles. Naukova Dumka, Kiev
53. Petrov YI (1986) Clusters and small particles. Nauka, Moscow
54. Gryaznov VG, Trusov LI (1993) Prog Mater Sci 37:289. doi:10.1016/0079-6425(93)90001-2
55. Khairutdinov RF (1998) Russ Chem Rev 67:109. doi:10.1070/RC1998v067n02ABEH000339
56. Gusev AI (1998) Nanocrystalline materials: methods of production and properties. Russian Academy of Sciences, Ekaterinburg
57. Morris DG (1998) Mechanical behaviour of nanostructured materials. In: Morris DG (ed) Materials science foundations, vol 2. Trans Tech Publications, Zurich
58. Andrievskii RA, Glezer AM (1999) Fiz Met Metalloved 88:50
59. Gusev AI, Rempel AA (2000) Nanocrystalline materials. Fizmatlit, Moscow
60. Gleiter H (2000) Acta Mater 48:1. doi:10.1016/S1359-6454(99)00285-2
61. Sun CQ (2007) Prog Solid State Chem 35:1. doi:10.1016/j.progsolidstchem.2006.03.001

62. Mei QS, Lu K (2008) Prog Mater Sci 52:1175. doi:10.1016/j.pmatsci.2007.01.001
63. Klabunde KJ (ed) (2001) Nanoscale materials in chemistry. Wiley, New York
64. Knauth P, Schoonman J (eds) (2004) Nanostructured materials. Selected synthesis methods, properties and applications. Kluwer, New York
65. Palatnik LS, Papirov II (1971) Epitaxial films. Nauka, Moscow
66. Morokhov ID, Trusov LI, Chizhik SP (1977) Ultradisperse metallic media. Atomizdat, Moscow
67. Uvarov NF, Brezhneva LI, Hairetdinov EF (2000) Solid State Ion 136–137:1273. doi:10.1016/S0167-2738(00)00587-7
68. Ponomareva VG, Lavrova GV (2001) Solid State Ion 145:197. doi:10.1016/S0167-2738(01)00957-2
69. Uvarov NF, Vanek P, Savinov M, Zelezny V, Studnicka V, Petzelt J (2000) Solid State Ion 127:253. doi:10.1016/S0167-2738(99)00288-X
70. Dubrovina AN, Akhtyamov YR, Knyazev EV, Ganelin VY, Trusov LI, Lapovok VN, Terekhov SB (1981) Kristallografia 26:410
71. Garvie RC (1965) J Phys Chem 69:1238. doi:10.1021/j100888a024
72. Zhang YL, Jin XJ, Ronga YH, Hsu TY, Jiang DY, Shi JL (2006) Mater Sci Eng A 438–440:399. doi:10.1016/j.msea.2006.03.109
73. Huber B, Brodyanski A, Scheib M, Orendorz A, Ziegler C, Gnaser H (2005) Thin Solid Films 472:114. doi:10.1016/j.tsf.2004.06.120
74. Uvarov NF, Khairetdinov EF, Bratel NB (1993) Russ J Electrochem 29:1231
75. Uvarov NF, Hairetdinov EF, Skobelev IV (1996) Solid State Ion 86–88:577. doi:10.1016/0167-2738(96)00208-1
76. Uvarov NF, Skobelev IV, Bokhonov BB, Hairetdinov EF (1996) J Mater Synth Process 4:391
77. Uvarov NF, Vanek P, Yuzyuk YI, Zelezny V, Studnicka V, Bokhonov BB, Dulepov VE, Petzelt J (1996) Solid State Ion 90:201. doi:10.1016/S0167-2738(96)00400-6
78. Lavrova GV, Ponomareva VG, Uvarov NF (2000) Solid State Ion 136–137:1285. doi:10.1016/S0167-2738(00)00590-7
79. Ponomareva VG, Lavrova GV, Uvarov NF, Hairetdinov EF (1996) Solid State Ion 90:161. doi:10.1016/S0167-2738(96)00410-9
80. Vinod MP, Bahnemann D (2002) J Solid State Electrochem 6:498. doi:10.1007/s10008-001-0251-6
81. Lee JS, Adams S, Maier J (2000) J Electrochem Soc 147:2407. doi:10.1149/1.1393545
82. Uvarov NF, Politov AA, Bokhonov BB (2000) Amorphization of ionic salts in nanocomposites. In: Chowdary BVR, Wang W (eds) Solid state ionics: materials and devices. World Science Publishing, Singapore, p 113
83. Uvarov NF (2000) Z Prikl Chem 73:413
84. Pavlov VA (1985) Fiz Metab Metalloved 59:629
85. Johnson WL (1986) Prog Mater Sci 30:81. doi:10.1016/0079-6425(86)90005-8
86. Avvakumov EG (1986) Mechanical methods of activation of chemical processes. Nauka, Novosibirsk
87. Koch CC (1989) Annu Rev Mater Sci 19:123
88. Serebryakov AV (1991) Metallofizika 13:115
89. Butyagin PY (1994) Russ Chem Rev 63:965. doi:10.1070/RC1994v063n12ABEH000129
90. Gusev VA, Gagarina VA, Moroz EM, Levitskii EA (1974) Kristallografiya 19:1289
91. Gusev VA, Gagarina VA, Moroz EM, Levitskii EA (1976) Kinet Katal 17:500
92. Aristov YI, Di Marco G, Tokarev MM, Parmon VN (1997) React Kinet. Catal Lett 61:147
93. Gordeeva LG, Restuccia G, Cacciola G, Aristov YI (1997) React Kinet Catal Lett 63:81
94. Gordeeva LG, Glaznev IS, Malakhov VV, Aristov YI (2003) Russ J Phys Chem 77:1843
95. Roman HE, Bunde A, Dietrich W (1986) Phys Rev B 34:3439. doi:10.1103/PhysRevB.34.3439
96. Roman HE, Yusouff M (1987) Phys Rev B 36:7285. doi:10.1103/PhysRevB.36.7285
97. Roman HE (1990) J Phys C Condens Matter 2:3909. doi:10.1088/0953-8984/2/17/002
98. Nan CW, Smith DM (1991) Mater Sci Eng B 10:99. doi:10.1016/0921-5107(91)90115-C
99. Uvarov NF, Ponomareva VG (1996) Dokl Russ Acad Sci 351:358
100. Uvarov NF, Hairetdinov EF, Bratel NB (1996) Solid State Ion 86–88:573. doi:10.1016/0167-2738(96)00207-X
101. Zhu B, Mellander BE (1994) Solid State Ion 70/71:285. doi:10.1016/0167-2738(94)90324-7
102. Lee JS, Maier J (1997) Interfacial phase transitions in AgI: Al2O3 composite electrolytes. In: Negro A, Montanaro L (eds) Proceedings of the International Conference EUROSOLID-97, Politechnico di Torino, p 115
103. Uvarov NF, Shastry MCR, Rao KJ (1990) Rev. Solid State Sci 4:61
104. Shastry MCR, Rao KJ (1992) Solid State Ion 51:311. doi:10.1016/0167-2738(92)90214-A
105. Tadanaga K, Imai K, Tatsumisago M, Minami T (2002) J Electrochem Soc 149:A773. doi:10.1149/1.1475687
106. Tadanaga K, Imai K, Tatsumisago M, Minami T (2000) J Electrochem Soc 147:4061. doi:10.1149/1.1394019
107. Phipps JB, Johnson DL, Whitmore DH (1981) Solid State Ion 5:393. doi:10.1016/0167-2738(81)90275-7
108. Fujitsu S, Kobayashi H, Koumoto K, Yanagida H (1986) J Electrochem Soc 133:1497. doi:10.1149/1.2108943
109. Fujitsu S, Miyayama M, Koumoto K, Yanagida H, Kanazawa T (1985) J Mater Sci 20:2103. doi:10.1007/BF01112293
110. Stoneham AM, Wade E, Kilner JA (1979) Mater Res Bull 14:661. doi:10.1016/0025-5408(79)90049-7
111. Wang JC, Dudney NJ (1986) Solid State Ion 18/19:112. doi:10.1016/0167-2738(86)90096-2
112. Dudney NJ (1985) J Am Ceram Soc 68:538. doi:10.1111/j.1151-2916.1985.tb11520.x
113. Brailsford AD (1986) Solid State Ion 21:159. doi:10.1016/0167-2738(86)90207-9
114. Mikrajuddin, Shi FG, Okuyama K (2000) J Electrochem Soc 147:3157
115. Jiang S, Wagner JB (1995) J Phys Chem Solids 56:1113. doi:10.1016/0022-3697(95)00026-7
116. Rojo AG, Roman HE (1988) Phys Rev B 37:3696. doi:10.1103/PhysRevB.37.3696
117. Bunde A, Dieterich W (2000) J Electroceram 5:81. doi:10.1023/A:1009997800513
118. Bunde A, Dieterich W, Roman E (1986) Solid State Ion 18/19:147. doi:10.1016/0167-2738(86)90102-5
119. Dieterich W (1989) Transport in ionic solids: Theoretical aspects. In: Takahashi T (ed) High conductivity conductors: solid ionic conductors. World Science Publishing, Singapore, p 17
120. Blender R, Dieterich W (1987) J Phys C Solid State Phys 20:6113. doi:10.1088/0022-3719/20/36/013
121. Knauth P, Debierre JM, Albinet G (1999) Solid State Ion 121:101. doi:10.1016/S0167-2738(98)00535-9
122. Siekierski M, Przyluski J (1994) Effective medium model for conductivity of composites. In: Chowdary BVR et al (ed) Solid state ionic materials. World Science Publishing, Singapore, p 121
123. Uvarov NF (1997) Dokl Russ Acad Sci 353:213
124. Uvarov NF (2000) Solid State Ion 136–138:1267. doi:10.1016/S0167-2738(00)00585-3
125. Lichtenecker K (1926) Phys Z 27:115
126. Landau LD, Lifshitz EM (1982) Electrodynamics of continuum media. Nauka, Moscow

127. Poulsen FM (1987) J Power Sources 20:317. doi:10.1016/0378-7753(87)80130-1
128. Chang MRW, Shahi K, Wagner JB (1984) J Electrochem Soc 131:1213. doi:10.1149/1.2115781
129. Maier J (1987) Solid State Ion 23:59. doi:10.1016/0167-2738(87)90082-8
130. Khaneft AV (2000) Z Nauch Prikl Fotogr 45:67
131. Qi WH, Wang MP (2003) Physica B 334:432. doi:10.1016/S0921-4526(03)00168-6
132. Suzdalev IP, Suzdalev PI (2001) Russ Chem Rev 70:177. doi:10.1070/RC2001v070n03ABEH000627
133. Bondarev VN, Kuklov AB (1985) Fiz Tverdogo Tela 27:3332
134. Gurevich YY, Kharkats Y (1978) J Phys Chem Solids 38:751
135. Boyce JB, Huberman BA (1979) Phys Rep 51:189. doi:10.1016/0370-1573(79)90067-X
136. Hainovsky N, Maier J (1995) Phys Rev B 51:15789. doi:10.1103/PhysRevB.51.15789
137. Catlow CRA (1997) Computer modeling in inorganic crystallography. Academic, New York
138. Huang Foen Chung RWJM, de Leeuw SW (2004) Solid State Ion 175:851. doi:10.1016/j.ssi.2004.09.047
139. Gainutdinov II, Uvarov NF (2006) Solid State Ion 177:1631. doi:10.1016/j.ssi.2006.05.026
140. Nomura K, Kobayashi M (2008) Ionics 14:131. doi:10.1007/s11581-007-0174-z
141. Sangster MJL, Dixon M (1976) Adv Phys 25:247. doi:10.1080/00018737600101392
142. Sata N, Ebermann K, Eberl K, Maier J (2000) Nature 408:946. doi:10.1038/35050047
143. Jin-Phillipp NY, Sata N, Maier J, Scheu C, Hahn K, Kelsch M, Ruhle M (2004) J Chem Phys 120:2375. doi:10.1063/1.1635809
144. Shukla AK, Manoharan R, Goodenough JB (1988) Solid State Ion 26:5. doi:10.1016/0167-2738(88)90238-X
145. Nakamura O, Saito Y (1992) Interfacial conductivities in Na4Zr2Si3O12/Insulator particle systems. In: Chowdary BVR et al (ed) Solid state ionics: materials and applications. World Science Publishing, Singapore, p 101
146. Saito Y, Asai T, Ado K, Nakamura O (1988) Mater Res Bull 23:1661. doi:10.1016/0025-5408(88)90256-5
147. Singh K, Lanje UK, Bhoga SS (1995) Ferroelectric and Al$_2$O$_3$ dispersed Li$_2$CO$_3$ composite solid electrolyte systems. Extended Abstracts: Tenth International Conference On Solid State Ionics, Singapore, p 112
148. Weston JE, Steele BCH (1982) Solid State Ion 7:75. doi:10.1016/0167-2738(82)90072-8
149. Croce F, Appetechi GB, Persi L, Scrosati B (1998) Nature 394:456. doi:10.1038/28818
150. Croce F, Scrosati B (2003) Ann N Y Acad Sci 984:194
151. Kumar B, Scanlon LG (1994) J Power Sources 52:261. doi:10.1016/0378-7753(94)02147-3
152. Stephan AM, Nahm KS (2006) Polymer (Guildf) 47:5952. doi:10.1016/j.polymer.2006.05.069
153. Wieczorek W, Florjancyk Z, Stevens JR (1995) Electrochim Acta 40:2251. doi:10.1016/0013-4686(95)00172-B
154. Przyluski J, Siekierski M, Wieczorek W (1995) Electrochim Acta 40:2101. doi:10.1016/0013-4686(95)00147-7
155. Panero S, Scrosati B, Greenbaum SG (1992) Electrochim Acta 37:1533. doi:10.1016/0013-4686(92)80106-V
156. Capiglia C, Mustarelli P, Quartarone E, Tomasi C, Magistris A (1999) Solid State Ion 118:73. doi:10.1016/S0167-2738(98)00457-3
157. Liu Y, Lee JY, Hong L (2004) J Power Sources 129:303. doi:10.1016/j.jpowsour.2003.11.026
158. Kim JW, Ji KS, Lee JP, Park JW (2003) J Power Sources 119–121:415. doi:10.1016/S0378-7753(03)00263-5
159. Kim YW, Lee W, Choi BK (2000) Electrochim Acta 45:1473. doi:10.1016/S0013-4686(99)00362-X
160. Sun HY, Takeda Y, Imanishi N, Yamamoto O, Sohn HS (2000) J Electrochem Soc 147:2462. doi:10.1149/1.1393554
161. Kumar B, Scanlon L, Marsh R, Mason R, Higgins R, Baldwin R (2001) Electrochim Acta 46:1515. doi:10.1016/S0013-4686(00)00747-7
162. Shaju KM, Chandra S (1995) J Mater Sci 30:3457. doi:10.1007/BF00349894
163. Arof AK (1994) J Phys III Fr 4:849. doi:10.1051/jp3:1994169
164. Agrawal RC, Kathal K, Gupta RK (1994) Solid State Ion 74:137. doi:10.1016/0167-2738(94)90203-8
165. Agrawal RC, Gupta RK (1997) J Mater Sci 32:3327. doi:10.1023/A:1018643910879
166. Agrawal RC, Verma ML, Gupta RK (1998) J Phys D 31:2854. doi:10.1088/0022-3727/31/20/020
167. Zabolotsky VI, Nikonenko VV (1996) Ionic transport in membranes. Nauka, Moscow
168. Yaroslavtsev AB, Nikonenko VV, Zabolotsky VI (2003) Russ Chem Rev 72:393. doi:10.1070/RC2003v072n05ABEH000797
169. Kreuer KD (2003) Hydrocarbon membranes. In: Vielstich W, Lamm A, Gasteiger H (eds) Fuel cell technology and applications. Handbook of fuel cells. fundamentals, technology and applications, vol. 3, part 3. Wiley, Chichester, p 420
170. Mustarelli P, Quartarone E, Tomasi C, Magistris A (2003) Solid State Ion 135:81. doi:10.1016/S0167-2738(00)00335-0
171. Colomban P (1992) Proton conductors: solids, membranes and gels—materials and devices. Cambridge University Press, Cambridge
172. Phipps JB, Whitmore DH (1983) Solid State Ion 9/10:123. doi:10.1016/0167-2738(83)90220-5
173. Slade RCT, Thomson IM (1988) Solid State Ion 26:287. doi:10.1016/0167-2738(88)90256-1
174. Ponomareva VG, Shutova ES (2007) Solid State Ion 178:729. doi:10.1016/j.ssi.2007.02.035
175. Matsui T, Kukino T, Kikuchi R, Eguchi K (2006) J Electrochem Soc 153:A339. doi:10.1149/1.2142211
176. Ponomareva VG, Lavrova GV, Burgina EB (2005) Solid State Ion 176:767. doi:10.1016/j.ssi.2005.09.021
177. Haile SM, Boysen DA, Chisholm CRI, Merle RB (2001) Nature 410:910. doi:10.1038/35073536
178. Lavrova GV, Russkih MV, Ponomareva VG, Uvarov NF (2005) Russ J Electrochem 41:640. doi:10.1007/s11175-005-0094-z
179. Lavrova GV, Russkih MV, Ponomareva VG, Uvarov NF (2006) Solid State Ion 177:2129. doi:10.1016/j.ssi.2006.03.025
180. Tatsumisago M, Shinkuma Y, Minami T (1991) Nature 354:217. doi:10.1038/354217a0
181. Tatsumisago M, Saito T, Minami T (1994) Solid State Ion 70/71:394. doi:10.1016/0167-2738(94)90343-3
182. Minami T, Saito T, Tatsumisago M (1996) Solid State Ion 86–88:415. doi:10.1016/0167-2738(96)00163-4
183. Adams S, Hariharan K, Maier J (1995) Solid State Ion 75:193. doi:10.1016/0167-2738(94)00219-I
184. Mizuno F, Hayashi A, Tadanaga K, Minami T, Tatsumisago M (2004) Solid State Ion 175:699. doi:10.1016/j.ssi.2004.08.027
185. Hayashi A, Komiya R, Tatsumisago M, Minami T (2002) Solid State Ion 152–153:285. doi:10.1016/S0167-2738(02)00313-2
186. Minami T, Hayashi A, Tatsumisago M (2006) Solid State Ion 177:2715. doi:10.1016/j.ssi.2006.07.017
187. Dudney NJ (1988) Solid State Ion 28–30:1065. doi:10.1016/0167-2738(88)90332-3
188. Despotuli AL, Nikolaichik VI (1993) Solid State Ion 60:275. doi:10.1016/0167-2738(93)90005-N
189. Tolstoy VP (2006) Russ Chem Rev 75:161. doi:10.1070/RC2006v075n02ABEH001197
190. Konisheva E, Neiman A, Gorbunova E (2003) Solid State Ion 157:45. doi:10.1016/0167-2738(02)00188-1

191. Neiman AYA, Pestereva NN, Sharafutdinov AR, Kostikov YUP (2005) Russ J Electrochem 41:598. doi:10.1007/s11175-005-0112-1

192. Hartmann E, Peller VV, Rogalski GI (1988) Solid State Ion 28–30:1098. doi:10.1016/0167-2738(88)90338-4

193. Hartmann E, Peller VV, Rogalski GI (1990) Solid State Ion 37:123. doi:10.1016/0167-2738(90)90235-J

194. Nemudry A, Rudolf P, Schöllhorn R (1996) Chem Mater 8:2232. doi:10.1021/cm950504+

195. Nemudry A, Goldberg EL, Aguirre M, Alario-Franco MA (2002) Solid State Sci 4:677. doi:10.1016/S1293-2558(02)01313-4

196. Nemudry A, Uvarov N (2006) Solid State Ion 177:2491. doi:10.1016/j.ssi.2006.05.002

197. Kresge CT, Leonowicz ME, Roth WJ, Vartuli JC, Beck JS (1992) Nature 359:710. doi:10.1038/359710a0

198. Fenelonov VB, Derevyankin AY, Kirik SD, Solovyov LA, Shmakov AN, Bonardet JL, Gedeon A, Romannikov VN (2001) Microporous Mesoporous Mater 44–45:33. doi:10.1016/S1387-1811(01)00166-4

199. Yamada H, Moriguchi I, Kudo T (2005) Solid State Ion 176:945. doi:10.1016/j.ssi.2004.11.013

200. Maekawa H, Tanaka R, Sato T, Fujimaki Y, Yamamura T (2004) Solid State Ion 175:281. doi:10.1016/j.ssi.2003.12.032

201. Maekawa H, Fujimaki Y, Shen H, Kawamura J, Yamamura T (2006) Solid State Ion 177:2711. doi:10.1016/j.ssi.2006.02.002

202. Subba Reddy CV, Wu GP, Zhao CX, Zhu QY, Chen W, Kalluru RR (2007) J Non-Cryst Solids 353:440. doi:10.1016/j.jnoncrysol.2006.12.010

203. Wang XL, Mei A, Li M, Lin Y, Nan CW (2006) Solid State Ion 177:1287. doi:10.1016/j.ssi.2006.06.016

204. Kim S, Hwang EJ, Park SJ (2008) Curr Appl Phys 8:729. doi:10.1016/j.cap.2007.04.028

205. Xi J, Qiu X, Ma X, Cui M, Yang J, Tang X, Zhu W, Chen L (2005) Solid State Ion 176:1249. doi:10.1016/j.ssi.2005.02.016

206. Lin YF, Yen CY, Ma CCM, Liao SH, Lee CH, Hsiao YH, Lin HP (2007) J Power Sources 171:388. doi:10.1016/j.jpowsour.2007.06.049

207. Uvarov NF, Ulihin AS, Slobodyuk AB, Kavun VY, Kirik SD (2008) ECS Trans 11(31):9. doi:10.1149/1.2953501

208. Yu C, Tian B, Zhao D (2003) Curr Opin Solid State Mater Sci 7:191. doi:10.1016/j.cossms.2003.10.004

209. Shigeoka H, Otomo J, Wen C, Ogura M, Takahashi H (2004) J Electrochem Soc 151:J76. doi:10.1149/1.1793192